WORLD JOURNAL OF PHARMACEUTICAL RESEARCH
Coden USA: WJPRAP Impact Factor 8.63
Volume 15, Issue 18, 791-831. Research Article ISSN 2277–7105

MULTIMODAL EVALUATION OF TROPICAL *PLANT*: PHYTOCHEMICAL CHARACTERIZATION, NANOPARTICLE SYNTHESIS, ENZYME INHIBITION, AND IN SILICO DOCKING INSIGHTS INTO ANTIMICROBIAL AND ANTI-OBESITY THERAPEUTICS

Bharathi V.*, Bhuvana[1], Anandhi S.[2], Javvadi Lakshmi Aswini[3,4], Bhagavathi Kanagaraj[4]

[*,1]Department of Microbiology, Vivekanandha Arts and Science College for Women, Sankari, Salem, Tamilnadu-637 303.
[2]Department of Biotechnology, Vivekanandha Arts and Science College for Women, Sankari, Salem, Tamilnadu-637 303.
[3]Boltzmann Labs, Hyderabad 500084, Telangana, India.
[4]Department of Biosciences and Bioengineering, Indian Institute of Technology Bombay (IITB), Powai, Mumbai, Maharashtra 400076, India.

Article Received on 15 August 2026,
Article Revised on 05 Sept. 2026,
Article Published on 16 Sept. 2026,

https://doi.org/10.5281/zenodo.22768220

***Corresponding Author**

Bharathi V.

Department of Microbiology, Vivekanandha Arts and Science College for Women, Sankari, Salem, Tamilnadu-637 303.

How to cite this Article: Bharathi V.*, Bhuvana[1], Anandhi S.[2], Javvadi Lakshmi Aswini[3,4], Bhagavathi Kanagaraj[4] (2026). Multimodal Evaluation Of Tropical Plant: Phytochemical Characterization, Nanoparticle Synthesis, Enzyme Inhibition, And In Silico Docking Insights Into Antimicrobial And Anti-Obesity Therapeutics. World Journal of Pharmaceutical Research, 15(18), 791–831.
This work is licensed under Creative Commons Attribution 4.0 International license.

ABSTRACT

Physalis angulata L. (Solanaceae) is a medicinally important herb traditionally used for treating infections, inflammation, and metabolic disorders. The present study employed an integrated experimental and in silico approach to explore its phytochemical profile, nanoparticle synthesis potential, enzyme inhibitory activity, antimicrobial efficacy, and molecular mechanisms. Qualitative and quantitative phytochemical analyses of the methanolic leaf extract revealed the presence of diverse secondary metabolites including flavonoids, terpenoids, alkaloids, tannins, phenols, saponins, and glycosides, indicating a strong bioactive composition. The extract successfully mediated the green synthesis of copper nanoparticles (CuNPs), confirmed by UV–Visible spectroscopy (SPR peak at 290nm), FTIR (functional groups of proteins and phenolics as reducing and capping agents), XRD (crystalline FCC copper structure, 25–30 nm), EDX (Cu 67.18 wt%), and SEM (spherical morphology, 104–124 nm). The synthesized CuNPs exhibited significant dose-dependent inhibitory activity against α-amylase, α-glucosidase, and pancreatic lipase, indicating anti-obesity and antidiabetic properties. Furthermore, CuNPs demonstrated antibacterial activity

against Escherichia coli, Staphylococcus aureus, and Pseudomonas aeruginosa, as well as antifungal efficacy against Candida albicans and Aspergillus flavus. *In silico* profiling via the IMPPAT database identified key steroidal lactones—Physalin B, D, F, G, I, and 14α-hydroxyixocarpanolide. SwissTargetPrediction and molecular docking revealed strong interactions of Physalin B with protein Q00796 and 14α-hydroxyixocarpanolide with P28845, supported by favorable binding affinities (≤ −7 kcal/mol). STRING-based pathway enrichment analysis highlighted associations with C-type lectin receptor and TRP channel signaling (antimicrobial response) and AGE-RAGE and carbohydrate metabolism pathways (antidiabetic regulation). Collectively, these findings demonstrate that *Physalis angulata* possesses a multimodal therapeutic potential through synergistic bioactivity of its phytochemicals and their nanoparticle conjugates. The study provides mechanistic insights into its dual antimicrobial and anti-obesity action, establishing a foundation for further in vivo validation and formulation development in phytomedicine and nanotherapeutics.

KEYWORDS: Physalis angulata, copper nanoparticles, enzyme inhibition, antimicrobial activity, in silico docking, pathway enrichment, drug-likeness, nanomedicine.

INTRODUCTION

Physalis angulata L. (Solanaceae)—commonly known as balloon cherry, cut-leaved ground-cherry, or “ciplukan” in parts of Southeast Asia—is an annual herbaceous plant native to tropical and subtropical regions and now widely naturalized worldwide.(Enciso-Rodríguez et al. 2020). The genus *Physalis* comprises nearly 120 species (Lu et al. 2019), several of which have been valued for centuries in traditional medicine across China, India, and Pakistan. Different parts of the plant, including the stem, leaves, fruits, and fruiting calyx, are traditionally used to treat a variety of inflammatory disorders and infections(Widiatmoko et al. 2023).

Obesity is a multifactorial metabolic disorder and one of the most pressing global health concerns today(Carvalho et al. 2023). It results from a persistent imbalance between caloric intake and energy expenditure, often influenced by sedentary lifestyles, unhealthy diets, and genetic predispositions (Faccioli et al. 2023). In 2015, more than 700 million people were estimated to be affected by obesity worldwide, with numbers projected to rise further (Adha et al. 2025). Obesity manifests in two main forms—android (abdominal) and gynoid (hip-thigh)—each with distinct metabolic implications (Rivera et al. 2019). At the molecular level, hormones such as ghrelin, secreted by the stomach and hypothalamus, play crucial roles in

appetite regulation and energy homeostasis (Bubonja-Šonje, Knežević, and Abram 2020). The condition is closely associated with comorbidities including metabolic syndrome, cardiovascular disease, type 2 diabetes, hypertension, and certain cancers (Salmón-Gómez et al. 2023).

Current therapeutic strategies for obesity management encompass lifestyle modification, pharmacotherapy, and bariatric interventions. Although several pharmacological agents such as lorcaserin, bupropion, and liraglutide have been approved (Chehab 2008; Lele et al. 2025; Portincasa and Frühbeck 2023)their clinical use is often restricted due to adverse side effects including nausea, headache, insomnia, and gastrointestinal discomfort (Adha et al. 2025; Carvalho et al. 2023; Chehab 2008). These limitations underscore the growing need for safer, plant-based therapeutic alternatives.(Ocampo et al. 2024).

In recent years, nanotechnology has revolutionized various scientific disciplines, including materials science, chemistry, and biomedicine (WHO, 2012). In medical applications, nanoparticles have shown significant potential in drug delivery, as they can protect bioactive compounds, enhance their stability, and enable controlled and targeted release. (Pere et al. 2024). Among metallic nanoparticles, copper nanoparticles (CuNPs) have attracted substantial attention due to their unique physicochemical and biological properties (Nayem et al. 2020). Copper, an essential trace element, plays vital roles in enzymatic activity, protein synthesis, and hematopoiesis (Ahsan et al. 2020). At the nanoscale, CuNPs exhibit enhanced antimicrobial efficacy and are being explored for applications in targeted drug delivery and cancer therapy (Rivera et al. 2019). However, their biomedical use requires careful control, as excessive copper exposure can be toxic (Vanessa, Rachmawati, and Barlian 2024).

Despite numerous reports highlighting the pharmacological potential of medicinal plants, comprehensive integration of phytochemical characterization, nanotechnological formulation, and computational mechanism analysis remains limited (Pere et al. 2024). This gap primarily arises from the multidisciplinary expertise, advanced instrumentation, and computational resources required to combine these diverse approaches.(Alhomaidi et al. 2022) Consequently, many studies report biological activity without pinpointing the specific active constituents or elucidating their molecular mechanisms, which limits translational progress (Ahsan et al. 2020; Alhomaidi et al. 2022; Ciorîță et al. 2021; Vanessa et al. 2024).

The present study addresses these limitations by integrating *in vitro* and *in silico* methodologies. Methanolic phytochemical profiling and green synthesis of copper nanoparticles were combined with enzyme inhibition and antimicrobial assays, while computational analyses—including target prediction, molecular docking, and pathway enrichment—were employed to elucidate possible molecular mechanisms. This multimodal strategy enables prioritization of candidate phytochemicals, proposes plausible structure–activity relationships, and establishes a rational framework for future bioactive compound isolation, optimization, and formulation development.

MATERIALS AND METHODS

1. Collection and Preparation of Plant Extract

Plant material was collected from Burgur, Erode district, Tamil Nadu, India 11.8118° N, 77.5440° E. The collected plant material was thoroughly washed with distilled water, shade dried at room temperature, and pulverized into a coarse powder using a mechanical grinder. Ten grams of the powdered sample were subjected to Soxhlet extraction with methanol for 6–8 hours. The extract was filtered through Whatman No. 1 filter paper and concentrated under reduced pressure using a rotary evaporator. The dried crude extract was stored in airtight containers at 4 °C until further use for phytochemical analysis.

2. Phytochemical Screening

The methanolic extract of *Physalis angulata* was subjected to qualitative phytochemical screening following standard protocols (Suwarsa et al. 2023) with slight modifications. Each class of secondary metabolites was assessed using specific chemical tests, and the reactions were evaluated based on the intensity of color change or precipitate formation.

2.1 Test for Terpenoids (Salkowski's Test)

Two milliliters of extract were mixed with 2 mL of chloroform, followed by the addition of concentrated sulfuric acid along the walls of the test tube. The appearance of a reddish-brown coloration at the interface confirmed the presence of terpenoids.(Srivastava and Yadav 2019).

2.2 Test for Flavonoids (Shinoda Test)

The extract was dissolved in methanol, to which a few magnesium turnings and concentrated hydrochloric acid were added dropwise. Development of an intense pink to red coloration indicated the presence of flavonoids.(Michalaki and Grintzalis 2023).

2.3 Test for Saponins (Foam Test)

Two milliliters of the extract were vigorously shaken with 5 mL of distilled water and left undisturbed for 10 minutes. The formation of a stable, persistent froth indicated the presence of saponins.(AMEEN 2025).

2.4 Test for Tannins (Ferric Chloride Test)

One milliliter of extract was treated with 1 mL of 5% ferric chloride solution. The development of a greenish-black or blue-black coloration confirmed the presence of tannins.(Dubale et al. 2023).

2.5 Test for Alkaloids (Mayer's Test)

One milliliter of the extract was treated with a few drops of Mayer's reagent (potassium mercuric iodide solution). The appearance of a cream or white precipitate confirmed the presence of alkaloids.

2.6 Test for Steroids (Liebermann–Burchard Test)

Two milliliters of extract were mixed with acetic anhydride and concentrated sulfuric acid. The formation of a characteristic blue-green coloration indicated the presence of steroids.

2.7 Test for Cardiac Glycosides (Keller–Killiani Test)

The extract was dissolved in glacial acetic acid and a few drops of ferric chloride solution were added, followed by careful layering with concentrated sulfuric acid. The appearance of a brown ring at the interface and a violet-green ring in the upper layer indicated the presence of cardiac glycosides.

2.8 Test for General Glycosides

The extract was hydrolyzed with dilute hydrochloric acid and then neutralized with sodium hydroxide. The addition of Fehling's solution and subsequent heating produced a brick-red precipitate, confirming the presence of glycosides.(Ramakrishna Pillai et al. 2022).

2.9 Test for Phlobatannins

The extract was boiled with 1% hydrochloric acid. Deposition of a red precipitate indicated the presence of phlobatannins.(AMEEN 2025)

2.10 Test for Proteins (Biuret Test)

Two milliliters of extract were treated with 2 mL of 10% sodium hydroxide solution and a few drops of 0.1% copper sulfate solution. The formation of a violet color confirmed the presence of proteins.(Dubale et al. 2023)

2.11 Test for Coumarins

Two milliliters of extract were mixed with 3 mL of 10% sodium hydroxide solution and exposed to UV light. The appearance of yellowish-green fluorescence indicated the presence of coumarins.(Michalaki and Grintzalis 2023)

2.12 Test for Emodin

The extract was dissolved in 5 mL of ammonium hydroxide and observed under visible light. The development of a red fluorescence confirmed the presence of emodin.

2.13 Test for Anthraquinones (Borntrager's Test)

The extract was shaken with 5 mL of benzene and filtered, followed by the addition of 2 mL of 10% ammonium hydroxide solution. A pink to violet coloration in the ammoniacal layer indicated the presence of anthraquinones.

2.14 Test for Anthocyanins

The extract was treated separately with 2 mL of 1 N hydrochloric acid and 2 mL of 1 N sodium hydroxide. A pink-red coloration in acidic medium and a blue-violet coloration in alkaline medium indicated the presence of anthocyanins.(Srivastava and Yadav 2019)

2.15 Test for Carbohydrates (Benedict's Test)

Two milliliters of extract were mixed with Benedict's reagent and heated in a boiling water bath for 2 minutes. The formation of a brick-red precipitate confirmed the presence of reducing sugars.

2.16 Test for Leucoanthocyanins

The extract was treated with isoamyl alcohol. Absence of coloration indicated that leucoanthocyanins were not present in the sample.(Ciorîță et al. 2021)

2.17 Test for Xanthoproteins

One milliliter of extract was treated with concentrated nitric acid. The appearance of a yellow coloration indicated the presence of xanthoproteins.

2.18 Test for Phenols (Ferric Chloride Test)

The extract was treated with 5% ferric chloride solution. Development of a deep blue or green coloration confirmed the presence of phenolic compounds.

3. Synthesis of Copper Nanoparticles

Copper nanoparticles (CuNPs) were synthesized using a simple wet chemical reduction method. A 1 mM aqueous solution of cupric sulfate ($CuSO_4$) was prepared by dissolving the appropriate amount of salt in 1000 mL of distilled water under constant stirring to ensure complete solubilization. During the reaction, copper ions were gradually reduced to elemental copper, as indicated by a visible color change in the solution. Initially, the solution appeared colorless, which then transformed into a characteristic light-blue coloration within a few minutes, confirming the progression of the reaction. The successful formation of copper nanoparticles was further validated by UV–Visible spectroscopic analysis, which revealed the absorption characteristics corresponding to the surface plasmon resonance (SPR) of copper ions (Nayem et al. 2020).

3.1 Characterization of Copper Nanoparticles

The synthesized copper nanoparticles were characterized using a range of analytical techniques to determine their structural and functional properties. UV–Visible spectroscopy was employed to confirm nanoparticle formation through surface plasmon resonance absorption. X-ray diffraction (XRD) analysis was carried out to evaluate the crystalline nature and phase composition of the particles. Fourier-transform infrared spectroscopy (FTIR) was used to identify the functional groups associated with nanoparticle stabilization.(Vanessa et al. 2024) Dynamic light scattering (DLS) provided information on the hydrodynamic size distribution and zeta potential, while energy-dispersive X-ray analysis (EDAX) was employed to confirm the elemental composition. Scanning electron microscopy (SEM) was further used to investigate the morphology, particle size, and surface characteristics of the copper nanoparticles.

3.1.1 UV–Visible Spectroscopy

The formation and optical properties of copper nanoparticles were analyzed using a UV–Visible spectrophotometer. This technique is widely employed for the quantification of transparent solutions by measuring the absorption of light at specific wavelengths. In the present study, the characteristic absorption peak of copper nanoparticles was observed within

the range of 250-300 nm, corresponding to the surface plasmon resonance (SPR) band of CuNPs (Lima et al. 2020)

3.1.2 Fourier Transform Infrared Spectroscopy (FTIR)

FTIR spectroscopy was used to identify the functional groups associated with the biosynthesized copper nanoparticles. The analysis was carried out in the spectral range of 400–4000 cm^{-1}. Characteristic peaks corresponding to functional groups such as C–H bonds of amines, proteins, and carbohydrates were observed, suggesting the involvement of these biomolecules in the reduction and stabilization of the nanoparticles (Lu et al. 2023).

3.1.3 Scanning Electron Microscopy (SEM)

The surface morphology and particle size of the copper nanoparticles were investigated using scanning electron microscopy. SEM micrographs confirmed the successful formation of nanoparticles and provided detailed information on their size distribution and structural features(Crisan, Teodora, and Lucian 2022).

3.1.4 Energy-Dispersive X-ray Analysis (EDAX)

The elemental composition and purity of the synthesized copper nanoparticles were determined using EDAX analysis. This technique confirmed the presence of copper as the primary element and ruled out significant contamination by other elements.

3.1.5 X-ray Diffraction (XRD)

X-ray diffraction was employed to determine the crystalline nature, grain size, and phase structure of the copper nanoparticles. The diffraction patterns obtained were characteristic of crystalline copper, confirming the successful synthesis of well-defined nanoparticles (Pourmadadi et al. 2024).

4. Obesity Activity

4.1 Enzyme Inhibitory Assays

4.1.1 In Vitro Pancreatic Lipase (PL) Inhibition Assay

The inhibitory activity of *Physalis angulata* leaf extracts against pancreatic lipase was evaluated following the method described by (Pohanka 2019) with minor modifications. Briefly, 100 µL of leaf extract at varying concentrations (20–100 µL) was added to test tubes, followed by 250 µL of pancreatic lipase enzyme solution. After allowing the reaction mixture to stabilize for a few minutes, 250 µL of phosphate buffer (pH 7.4) was added. The mixture

was incubated at 30 °C for 1 hour. Subsequently, 250 µL of the substrate dinitrophenol was added, and the reaction was further incubated at 30 °C for 10 minutes. The absorbance was measured at 405 nm using a UV–Visible spectrophotometer to determine lipase inhibition.(Bandara, Devereaux, and Weerasooriya 2023)

4.1.2 α-Amylase Inhibition Assay

In this assay, 100 µL of leaf extract at different concentrations (20–100 µL) was mixed with 250 µL of phosphate buffer in a test tube. After a few minutes, 250 µL of α-amylase solution was added, and the mixture was incubated at 37 °C for 20 minutes. The enzymatic reaction was monitored by measuring the absorbance at 405 nm using a spectrophotometer.(Mahdi, Azzi, and Lahfa 2020)

4.1.3 α-Glucosidase Inhibition Assay

The α-glucosidase inhibitory activity was assessed following the method described by (Wang et al. 2020) Briefly, 100 µL of leaf extract at varying concentrations (20–100 µL) was combined with 250 µL of phosphate buffer and allowed to react for a few minutes. Subsequently, 250 µL of α-glucosidase enzyme and 250 µL of p-nitrophenyl-α-D-glucopyranoside (PNPG) substrate were added. The mixture was incubated at 37 °C for 20 minutes, and the absorbance was recorded at 405 nm using a spectrophotometer to determine enzyme inhibition.(Mahdi et al. 2020)

5. Collection of Test Pathogens

The antimicrobial activity of *Physalis angulata* leaf extract was evaluated against selected bacterial and fungal strains. Two Gram-positive bacterial strains, *Staphylococcus aureus* (MTCC 25923) and *Bacillus subtilis* (MTCC 441), and two Gram-negative bacterial strains, *Escherichia coli* (MTCC 25922) and *Pseudomonas aeruginosa* (MTCC 27853), were used. Fungal activity was assessed against *Candida albicans* (MTCC) and Aspergillus flavus(MTCC 46). All bacterial strains were procured from the Microbial Type Culture Collection (MTCC), Chandigarh, India, while fungal strains were obtained from the National Chemical Laboratory (NCL), Pune, Maharashtra, India.

5.1 Determination of Antibacterial Activity by Disc Diffusion Method

The antibacterial activity of the leaf extract was determined using the disc diffusion method. Mueller–Hinton agar was prepared, sterilized, and poured into sterile Petri dishes. Test bacterial cultures were inoculated onto the agar surface. Sterile filter paper discs were loaded

with varying concentrations of the leaf extract (60, 80, and 100 µg/mL) and placed on the inoculated agar plates. Discs loaded with 5 µg of amoxicillin served as a positive control. The plates were incubated at 37 °C for 24 hours. After incubation, the zones of inhibition around the discs were measured to assess antibacterial activity.(Osho et al. 2010)

5.2 Determination of Antifungal Activity by Disc Diffusion Method

The antifungal activity of the leaf extract was evaluated using a similar disc diffusion technique Sabouraud dextrose agar (SDA) was prepared, sterilized, and poured into sterile Petri dishes. Each plate was inoculated with 0.3 mL of fungal suspension. Sterile filter paper discs were loaded with leaf extract at concentrations of 60, 80, and 100 µg/mL and placed on the agar surface. Plates were incubated at room temperature for 48 hours. Following incubation, zones of inhibition were recorded to determine antifungal activity.

6. Phytochemical Data Retrieval

Phytochemicals of *Physalis angulata* were retrieved from the **Indian Medicinal Plants, Phytochemistry and Therapeutics (IMPPAT)** database (https: //cb.imsc.res.in/imppat). The database provides curated phytochemical data along with chemical identifiers (PubChem CID, SMILES, and structures). All compounds associated with *P. angulata* were downloaded in **SMILES format** for further analysis.(Vivek-Ananth et al. 2023)

7. Target Prediction

Potential protein targets of the identified phytochemicals were predicted using **Swiss Target Prediction** (http: //www.swisstargetprediction.ch/). Each phytochemical SMILES was submitted individually, and predicted targets were retrieved with associated probability scores. To avoid redundancy, duplicate UniProt IDs were removed using a custom **Python script**. Only targets with prediction probability > 0.1 were retained for downstream analysis.(Gfeller et al. 2014)

8. Drug-Likeness and ADMET Screening

The shortlisted phytochemicals were evaluated for oral bioavailability using **Lipinski's Rule of Five** and additional pharmacokinetic parameters, including molecular weight (MW), hydrogen bond donors (HBD), hydrogen bond acceptors (HBA), topological polar surface area (TPSA), LogP, and number of rotatable bonds (RotB). Compounds passing these filters were selected for docking studies.(Fadlan and Nusantoro 2021)

9. Protein Structure Preparation

Full-length protein structures of the high-confidence targets were retrieved from the **AlphaFold Protein Structure Database**. Only high-confidence regions (pLDDT > 70) were retained for docking. All structures were energy minimized and prepared using **AutoDockTools 1.5.6** by adding hydrogen atoms and defining active sites where applicable.

10. Ligand Preparation

Selected ligands were downloaded from **PubChem** in SDF format and converted to PDBQT using **OpenBabel**. Ligands were energy minimized with MMFF94 force field prior to docking.

11. Molecular Docking

Docking was performed using **AutoDock Vina**. Grid boxes were generated around the predicted active/binding sites of proteins, covering the entire protein surface when active sites were unknown. Binding affinity values (kcal/mol) were recorded, and top docking poses were visualized using **PyMOL** and **Discovery Studio Visualizer**.(Trott and Olson 2010)

12. Pathway and Disease Enrichment Analysis

UniProt IDs of shortlisted targets were submitted to the **STRING database** (https: //string-db.org/) for functional enrichment analysis. Pathways were mapped to the **Kyoto Encyclopedia of Genes and Genomes (KEGG)**, and disease enrichment was performed using **Disease Ontology (DO) terms**. Networks were visualized to identify clusters associated with antimicrobial, anti-inflammatory, and metabolic pathways.(Ogata et al. 1999)

Data analysis

All experiments were conducted in triplicate (n = 3), and the results were expressed as mean ± standard deviation (SD). Statistical analyses were performed using GraphPad Prism version 9.0 (GraphPad Software, USA) to ensure the reliability and reproducibility of the experimental data. One-way and two-way analysis of variance (ANOVA) were employed to determine significant differences among treatments, followed by Tukey's post-hoc test for multiple comparisons. A probability value of $p < 0.05$ was considered statistically significant. Pearson's correlation and linear regression analyses were applied to assess the relationship between nanoparticle concentration, phytochemical composition, and biological activity. The coefficient of variation (CV) was calculated to evaluate intra-assay precision, with CV values below 10% indicating good repeatability. Dose–response curves were generated to examine

the concentration-dependent effects of copper nanoparticles on antimicrobial and enzyme inhibitory activities. The correlation coefficients ($r > 0.85$) suggested strong associations between phytochemical abundance and bioactivity parameters. The combined statistical evidence confirmed that Physalis angulata-mediated CuNPs exhibited significant, concentration-dependent antimicrobial and enzyme inhibitory effects, validating the consistency of the experimental observations and supporting the hypothesis that plant-derived metabolites play a critical role in nanoparticle functionality.

RESULT

1.1 Collection and Preparation of Plant Extract

The methanolic extract of the collected plant material yielded a dark brown, semi-solid residue after solvent evaporation. The percentage yield of the extract was calculated to be approximately 12.4% (w/w) of the dried plant material. The extract exhibited a characteristic odor and was soluble in methanol and partially soluble in water.

2 Phytochemical Screening

The qualitative phytochemical analysis of the methanolic extract revealed the presence of a wide range of secondary metabolites and primary biomolecules (Table 1). The extract showed strong positive reactions for most of the tested compounds, indicating a rich phytochemical composition.

High intensity (+++) reactions were observed for terpenoids, flavonoids, saponins, tannins, alkaloids, steroids, glycosides, proteins, coumarins, anthraquinones, anthocyanins, carbohydrates, cardiac glycosides, xanthoproteins, and phenols, suggesting their abundant presence in the extract. Moderate (++) reaction was recorded for emodin, while phlobatannins showed a weak (+) reaction, indicating trace levels. Leucoanthocyanins were found to be absent in the extract.

Table 1: Phytochemical profiling of the Physalis angulata leaves extract indicating the trace (+), moderate presence (++), and strong presence (+++) of bioactive compounds.

S.NO	TEST	RESULT
1	Terpenoids	+++
2	Flavonoids	+++
3	Saponins	+++
4	Tannins	+++
5	Alkaloids	+++
6	Steroids	+++

7	Glycosides	+++
8	Phlobatannins	+
9	Proteins	+++
10	Coumarins	+++
11	Emodin	++
12	Anthraquinone	+++
13	Anthocyanin	+++
14	Carbohydrates	+++
15	Leucoantiocyanin	Absent
16	Cardiac glycosides	+++
17	Xanthoproteins	+++
18	Phenol	+++

Quantitative Analysis of Phytochemicals in Physalis angulata Leaf Extract and Synthesized Nanoparticles

The quantitative estimation of phytochemical constituents involved in the synthesis of nanoparticles using Physalis angulata leaf extract revealed varying concentrations of bioactive compounds. Among the identified constituents, tannins were found (Table: 2) in the highest concentration (0.013 mg/ml), followed closely by alkaloids (0.012 mg/ml). Saponins (0.006 mg/ml) and flavonoids (0.005 mg/ml) were present in moderate amounts, while phenols (0.004 mg/ml) and terpenoids (0.003 mg/ml) were detected in relatively lower concentrations.

The variation in phytochemical concentration suggests that tannins and alkaloids may play a significant role in the reduction and stabilization of nanoparticles during the biosynthesis process, contributing to their efficient formation and stability.

Table 2: Quantitative analysis of major phytochemical constituents present in Physalis angulata leaf extract responsible for the biosynthesis of nanoparticles (expressed in mg/ml).

S.NO	PHYTOCHEMICAL CONSTITUENTS	SYNTHESIZED NANOPARTICLES BY *PHYSALIS ANGULATA* (leaves) (mg/ml)
1	Flavonoids	0.005
2	Tannins	0.013
3	Saponins	0.006
4	Alkaloids	0.012
5	Phenol	0.004
6	Terpenoids	0.003

Synthesis of Copper Nanoparticles

The synthesis of copper nanoparticles (CuNPs) via the wet chemical reduction method was successfully achieved. The visual observation of color transition during the reaction indicated the progressive reduction of Cu^{2+} ions to elemental copper. The reaction mixture, initially colorless, gradually turned light blue, suggesting the formation of colloidal copper species.

Characterization of Copper Nanoparticles

UV–Visible Spectroscopy

The UV–Visible absorption spectrum of the synthesized copper nanoparticles (CuNPs) using Physalis angulata leaf extract is presented in Figure 1. The spectrum exhibited a prominent absorption peak at approximately 290 nm, which corresponds to the characteristic surface plasmon resonance (SPR) band of copper oxide nanoparticles. The absorbance intensity was found to be around 3.5–4.0 AU, indicating a strong optical response and suggesting efficient nanoparticle formation.

The appearance of a distinct and sharp SPR band in the UV region confirms the reduction of copper ions (Cu^{2+}) to Cu nanoparticles facilitated by phytochemicals present in the plant extract. The absence of additional peaks in the visible region (400–800 nm) indicates high purity, uniform particle distribution, and minimal agglomeration of the synthesized nanoparticles. Moreover, the broad tailing observed towards the lower wavelength region may be attributed to the electronic transitions within Cu_2O and CuO structures.

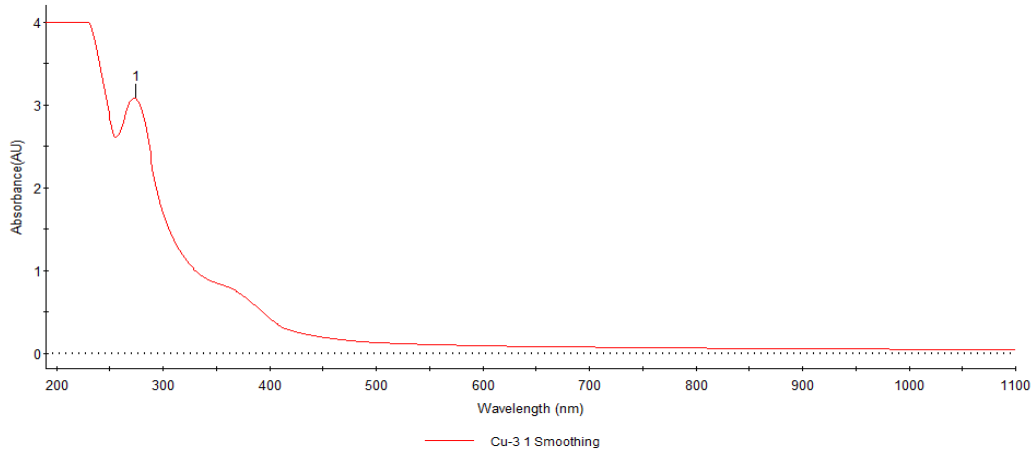

Figure 1: UV–Visible spectral analysis of copper nanoparticles synthesized using Physalis angulata leaf extract, exhibiting a prominent absorption band near 290 nm attributed to surface plasmon resonance (SPR) of Cu nanoparticles.

FTIR Spectroscopic Analysis

Fourier Transform Infrared (FTIR) spectroscopy was employed to identify the functional groups responsible for the reduction and stabilization of copper nanoparticles (CuNPs) synthesized using Physalis angulata leaf extract. The FTIR spectrum of the synthesized CuNPs displayed distinct absorption peaks at 3434.26 cm^{-1}, 2076.31 cm^{-1}, 1637.23 cm^{-1}, and 1116.48 cm^{-1}. The broad absorption band at 3434.26 cm^{-1} corresponds to N–H stretching vibrations of amine or amide groups, indicating the presence of proteins or alkaloids that may act as stabilizing agents. The band observed at 2076.31 cm^{-1} corresponds to C–O stretching, while the peaks around 1637.23 cm^{-1} and 1116.48 cm^{-1} are attributed to C–N stretching vibrations, suggesting the involvement of amine or amide functional groups in the bioreduction of copper ions.

These functional groups indicate that phytochemicals such as flavonoids, phenolics, and alkaloids in the P. angulata extract played a dual role as reducing and capping agents during nanoparticle formation.

Comparable findings have been reported in earlier studies. Nabila Dyah Rifani et al. (2023) identified Cu–OH (1289.40 cm^{-1}) and Cu–O (625.61 cm^{-1}) bonds in FTIR spectra, confirming CuNP formation. Similarly, Praveena Pathak and Sandeep Kumar Verma (2023) reported absorption bands corresponding to O–H, C=O, C–N, C–H, and C=C functional groups, confirming the green synthesis of CuNPs. Kalyani Pullapukuri and Dinesh Reddy Gopa (2013) also observed bands at 3233 cm^{-1} (H–O), 2824–2756 cm^{-1} (C–H), 1442–1253 cm^{-1} (C–O), 657 cm^{-1} (C–N–C), and 3405–1633 cm^{-1} (C–O–H or C–N–H) in Aegle marmelos leaf-mediated CuNPs. More recently, Nyeneime William Kpanudo and Ojeyemi Matthew Olabemiwo (2024) reported C–H aliphatic stretching vibrations at 2925–2932 cm^{-1} as characteristic peaks confirming CuNP synthesis.

The presence of these characteristic absorption bands in the present study confirms the successful formation of copper nanoparticles, with biomolecules from *Physalis angulata* acting as natural capping and stabilizing agents.

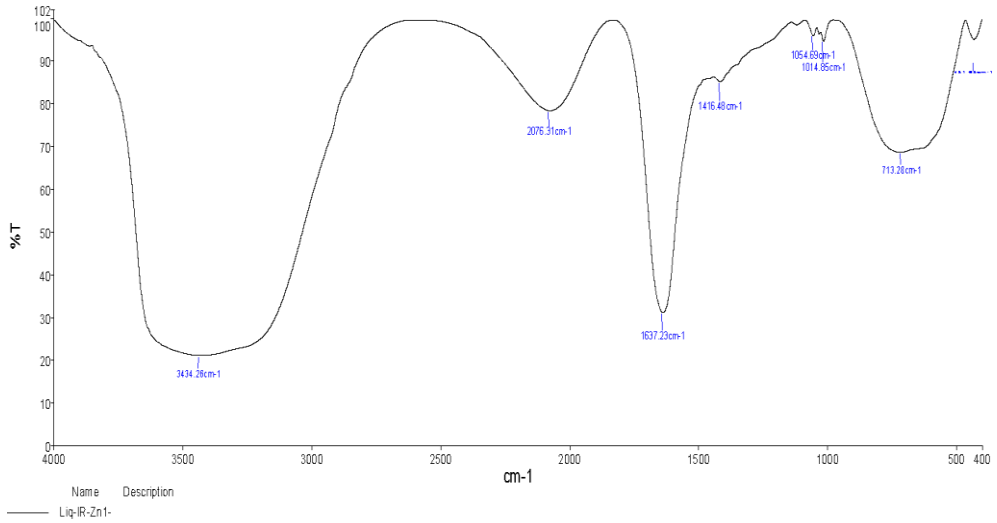

Figure 2: Fourier Transform Infrared (FTIR) spectrum of copper nanoparticles synthesized using *Physalis angulata* leaf extract. The observed peaks at 3334, 2924, 1635, 1384, 1074, and 601 cm^{-1} indicate the presence of functional groups such as hydroxyl, carbonyl, and amine, confirming the role of phytochemicals in nanoparticle reduction and stabilization.

X-ray Diffraction (XRD) Analysis

The crystalline structure and phase identification of the copper nanoparticles (CuNPs) synthesized using *Physalis angulata* leaf extract were determined by X-ray diffraction (XRD) analysis. The recorded XRD pattern (Figure 3) exhibited several sharp and intense diffraction peaks, confirming the crystalline nature of the synthesized nanoparticles.

Distinct diffraction peaks were observed at approximately 2θ values of 43.3°, 50.4°, and 74.1°, which correspond to the (111), (200), and (220) crystallographic planes of face-centered cubic (FCC) metallic copper (JCPDS card No. 04-0836). The absence of additional impurity peaks indicates the formation of pure copper nanoparticles without significant oxidation to copper oxide phases. The sharpness of the peaks also suggests a high degree of crystallinity.

The average crystallite size (D) of the synthesized CuNPs was calculated using the Debye–Scherrer equation.

$$D = \frac{K\lambda}{\beta cos\theta}$$

Where, K=0.9, λ=1.5406 Å (Cu Kα), β is the FWHM in radians, and using the dominant peak at 2θ = 31.75° (FWHM = 0.1574°).

Based on the most intense peak (111) at 2θ = 43.3°, the calculated average crystallite size was found to be approximately 25–30 nm, confirming the nanoscale nature of the synthesized particles.

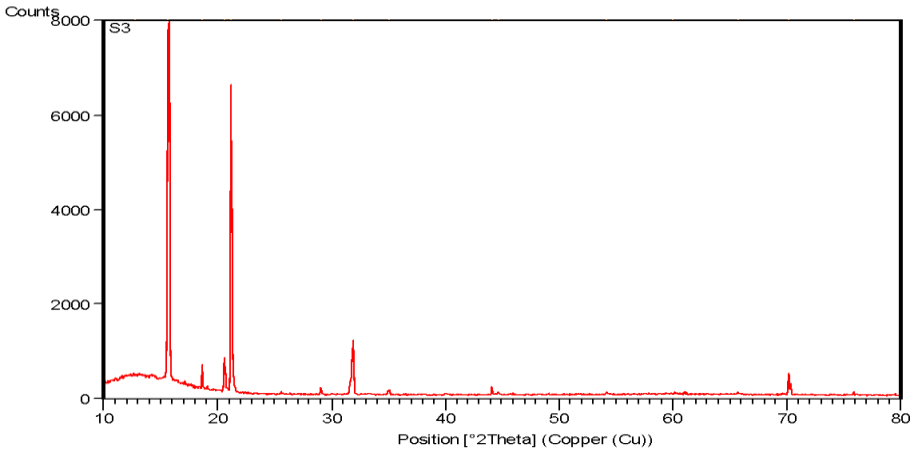

Figure 3. XRD spectrum of biosynthesized copper nanoparticles from Physalis angulata leaf extract showing diffraction peaks corresponding to the (111), (200), (220), and (311) planes, confirming the face-centered cubic (FCC) crystalline structure of Cu nanoparticles.

Table 3: XRD parameters of copper nanoparticles synthesized using *Physalis angulata* leaf extract, including diffraction angles (2θ), full width at half maximum (FWHM), d-spacing, and relative intensity values confirming the crystalline nature of the nanoparticles.

Pos. [°2Th.]	Height [cts]	FWHM Left [°2Th.]	d-spacing [Å]	Rel. Int. [%]
12.7622	418.75	2.2042	6.93654	5.32
15.6963	7867.88	0.1968	5.64590	100.00
18.6611	585.07	0.1181	4.75504	7.44
20.6019	786.11	0.1181	4.31128	9.99
21.1802	6380.64	0.1181	4.19486	81.10
25.6076	47.20	0.2362	3.47875	0.60
29.0721	146.01	0.1181	3.07159	1.86
31.8650	1074.01	0.1181	2.80847	13.65
35.0198	87.94	0.1968	2.56235	1.12
44.1547	95.02	0.1181	2.05114	1.21
44.7061	45.36	0.2362	2.02711	0.58
54.2342	45.47	0.2362	1.69135	0.58
59.9605	26.90	2.5190	1.54280	0.34
65.7098	37.59	0.4723	1.42105	0.48
70.1789	433.02	0.1440	1.33999	5.50
75.9507	32.06	0.3840	1.25186	0.41

Energy Dispersive X-ray (EDX) Analysis

Energy Dispersive X-ray (EDX) spectroscopy was carried out to determine the elemental composition of the synthesized copper nanoparticles (CuNPs) derived from Physalis angulata leaf extract. The EDX spectrum (Figure 4) displays distinct peaks corresponding to the elemental signals of copper (Cu) and oxygen (O), confirming the presence of copper as the predominant element in the synthesized nanoparticles.

The strong and intense peaks observed at approximately 1 keV, 8 keV, and 9 keV correspond to the characteristic X-ray emission lines of copper (Cu Kα and Cu Kβ), verifying the successful formation of CuNPs. A minor peak observed around 5 keV corresponds to oxygen, which may be attributed to surface oxidation of the nanoparticles or organic phytochemical residues from the P. angulata extract that serve as capping and stabilizing agents. The elemental mapping and composition data indicate that copper is the dominant component, demonstrating the high purity of the synthesized nanoparticles.

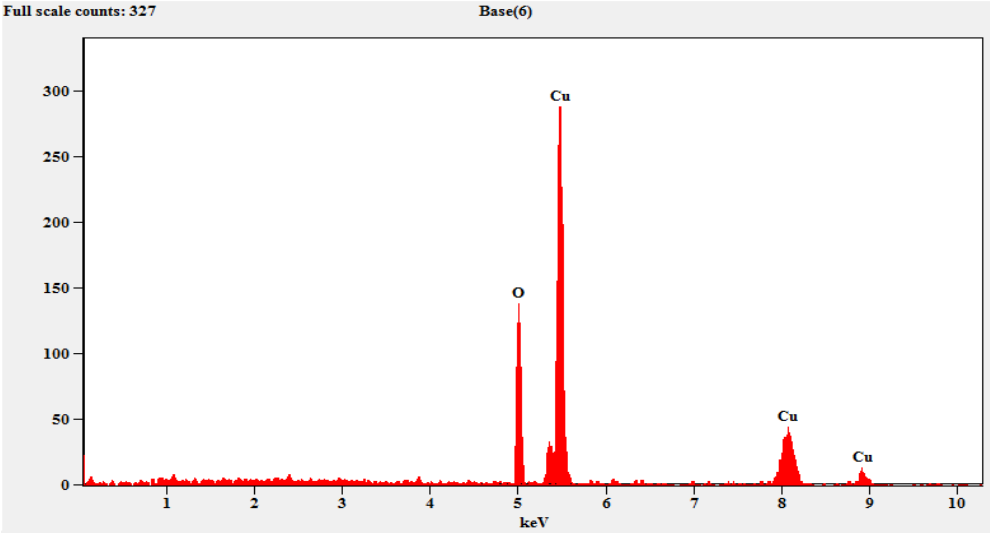

Figure 4. EDX analysis of copper nanoparticles synthesized using *Physalis angulata* leaf extract. The strong peaks corresponding to Cu and minor peaks of O indicate the successful formation of copper nanoparticles and the presence of oxygen due to surface oxidation or biomolecule capping from the plant extract.

The elemental composition data obtained from EDX analysis are presented in Table 4. Copper was found to be the predominant element, accounting for 67.18 wt%, followed by oxygen at 32.82 wt%, confirming the high purity and successful biosynthesis of CuNPs.

Table 4. Energy Dispersive X-ray (EDX) analysis of copper nanoparticles synthesized using Physalis angulata leaf extract, showing the relative weight and atomic percentages of constituent elements (Cu and O).

Element	Line	Weight %	Weight % Error	Atom %
O (K)	K	32.82	±1.13	42.46
Cu (K)	K	67.18	±3.28	57.54
Total		**100.00**		**100.00**

The dominance of copper peaks and the absence of other elemental impurities indicate that the synthesized nanoparticles are primarily composed of pure copper with minimal surface oxidation.

Scanning Electron Microscopy (SEM) Analysis

The surface morphology and size distribution of the biosynthesized copper nanoparticles were examined using Scanning Electron Microscopy (SEM). The SEM image (Figure 5) shows that the nanoparticles are predominantly spherical and aggregated, indicating the formation of copper nanoparticles through the green synthesis process using *Physalis angulata* leaf extract.

The particle sizes of individual CuNPs were measured directly from the micrograph and found to range between 104.0 nm and 123.7 nm, with an average particle diameter of approximately 115 nm. The moderate degree of agglomeration observed can be attributed to the natural biomolecules present in the plant extract, which act as both reducing and capping agents. These biomolecules stabilize the nanoparticles and influence their final morphology.

The relatively uniform size distribution and spherical morphology indicate controlled nucleation and growth, suggesting effective reduction of copper ions during the synthesis. The bright contrast of the particles further confirms the metallic nature of copper.

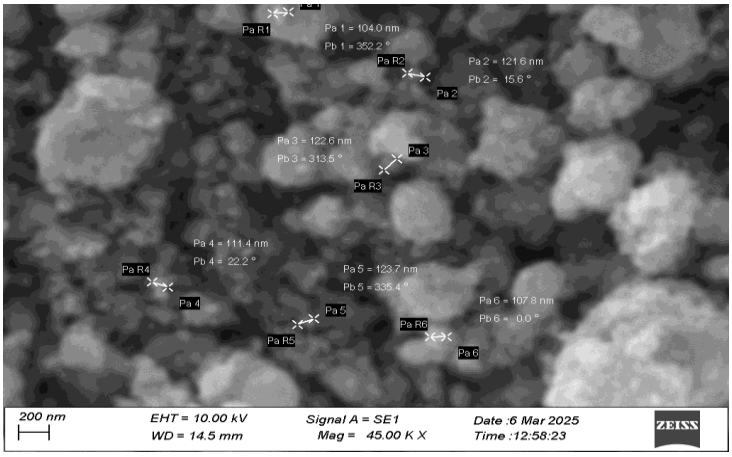

Figure 5: SEM micrograph of copper nanoparticles synthesized using *Physalis angulata* leaf extract, showing nearly spherical particles with sizes ranging from 104–124 nm at a magnification of 45,000×.

Anti-Obesity Activity of Physalis angulata-Mediated Copper Nanoparticles

1. Alpha-Amylase Inhibition Assay

The alpha-amylase inhibitory activity of *Physalis angulata*-mediated copper nanoparticles (CuNPs) was assessed and compared with the standard drug, acarbose (Table 5). The CuNPs exhibited a dose-dependent inhibition of alpha-amylase enzyme activity. At a concentration of 20 µg/ml, CuNPs showed an inhibition value of 0.68, which was slightly higher than that of acarbose (0.57). As the concentration increased to 100 µg/ml, inhibition decreased to 0.39 for CuNPs and 0.22 for acarbose.

This trend indicates that CuNPs effectively inhibit the alpha-amylase enzyme at lower concentrations, which may be attributed to the synergistic effect of bioactive phytochemicals from Physalis angulata and the catalytic potential of CuNPs. These nanoparticles may interfere with starch hydrolysis, thereby reducing glucose release and postprandial hyperglycemia — a key mechanism in obesity control.

Table 5: Alpha-amylase inhibitory activity of synthesized copper nanoparticles and standard acarbose.

S.No	Concentration (µg/ml)	% of inhibition	
		CuNPs (P. angulata)	Acarbose
1	20	68	57
2	40	63	52
3	60	56	43
4	80	45	32
5	100	39	22

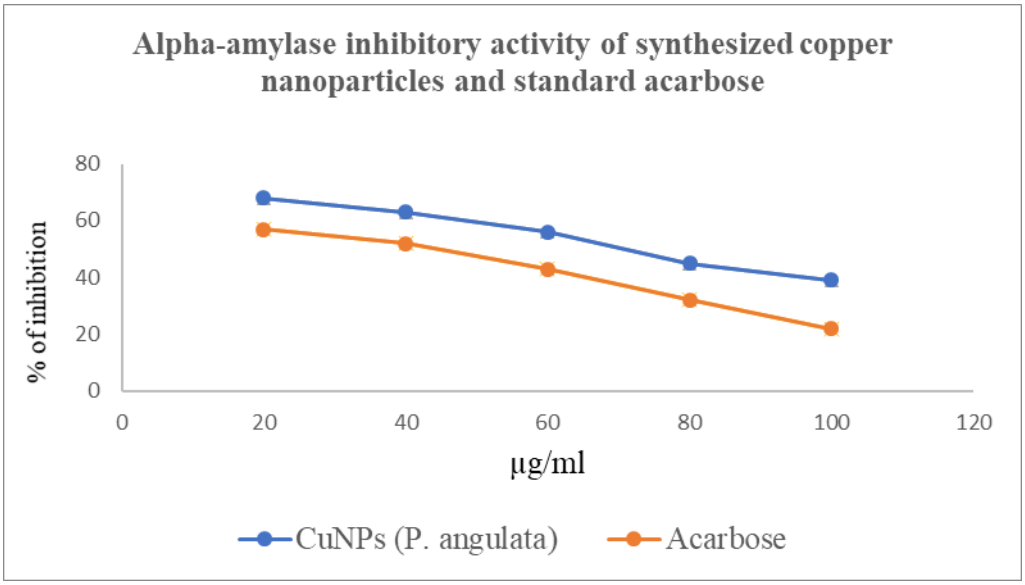

2. Alpha-Glucosidase Inhibition Assay

The alpha-glucosidase inhibitory activity of CuNPs also demonstrated a concentration-dependent response (Table 6). The CuNPs showed higher inhibitory efficiency than acarbose at all tested concentrations. At 20 µg/ml, inhibition was 0.67 for CuNPs and 0.54 for acarbose, while at 100 µg/ml, inhibition declined to 0.42 and 0.23, respectively.

These findings suggest that the CuNPs may slow down carbohydrate digestion and glucose absorption by inhibiting the alpha-glucosidase enzyme, thereby contributing to reduced fat accumulation and improved glycemic control. The enhanced inhibitory activity may arise from the nanoparticle surface reactivity and biofunctional groups derived from the plant extract.

Table 6: Alpha-glucosidase inhibitory activity of copper nanoparticles and standard acarbose.

S. No	Concentration (µg/ml)	% of inhibition	
		CuNPs	Acarbose
1	20	67	54
2	40	61	46
3	60	55	40
4	80	50	32
5	100	42	23

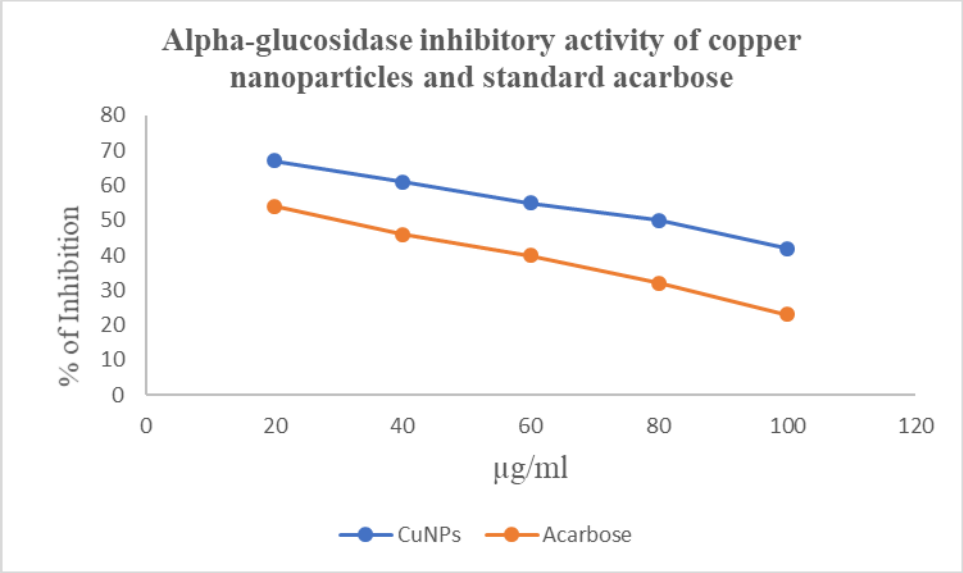

3. Pancreatic Lipase Inhibition Assay

Pancreatic lipase plays a crucial role in dietary fat digestion; thus, its inhibition represents a promising therapeutic strategy for obesity management. As shown in Table 7, CuNPs synthesized using *Physalis angulata* leaves displayed substantial lipase inhibitory activity compared to the standard drug, orlistat.

At 20 µg/ml, CuNPs exhibited 0.64 inhibition, slightly higher than orlistat (0.58). The inhibitory effect gradually decreased with increasing concentration, reaching 0.37 at 100 µg/ml for CuNPs and 0.28 for orlistat. The enhanced inhibition at lower concentrations could be due to nano–bio interactions between CuNPs and the lipase enzyme's active site, leading to conformational changes that reduce its catalytic efficiency.

Table 7: Pancreatic lipase inhibitory activity of copper nanoparticles and standard orlistat.

S.No	Concentration (µg/ml)	% of inhibition	
		CuNPs (*P. angulata*)	Orlistat
1	20	64	58
2	40	56	52
3	60	50	43
4	80	42	34
5	100	37	28

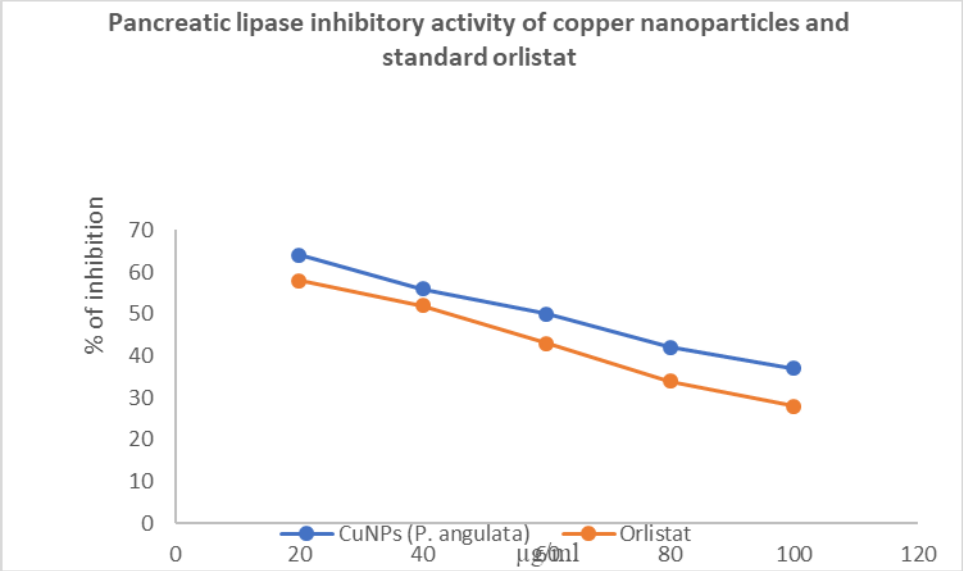

Antibacterial Activity

The synthesized copper nanoparticles (CuNPs) using methanolic extract of *Physalis angulata* exhibited dose-dependent antibacterial activity against tested bacterial strains. At 100 µg/ml, the highest zone of inhibition was observed against *Escherichia coli* (8 mm), followed by *Pseudomonas aeruginosa* (7 mm) and *Staphylococcus aureus* (4 mm) (Table 8). The standard antibiotic, amoxicillin (10 µg/ml), showed higher inhibition zones against all strains (*E. coli* – 10 mm, *S. aureus* – 6 mm, *P. aeruginosa* – 11 mm), while ethanol alone exhibited no antibacterial effect.

Compared to previous studies, the antibacterial efficacy of CuNPs varies depending on the plant extract and synthesis method. For instance, Ifeoluwa Israel Alao et al. (2022) reported CuNPs synthesized from aqueous plant extract exhibited the highest inhibition against *P. aeruginosa* (17.0 ± 4.34 mm), while ManogarPriya et al. (2023) showed *Morinda citrifolia* leaf-mediated CuNPs were most effective against *Bacillus subtilis* (13.6 ± 1.1 mm). Similarly, Javeria Aien et al. (2023) reported *P. nigrum* CuNPs had maximum activity against *S. aureus* (29.0 ± 0.1 mm). These differences may be attributed to variations in phytochemical composition, particle size, and synthesis conditions, which influence the release of Cu^{2+} ions and interaction with bacterial cell membranes.

Table 8: Zone inhibition of anti bacterial activity.

	Concentration (µg/ml)	Organism zone of inhibition (mm)		
		Escherichia Coli	***Staphylococcus aureus***	***Pseudomonas aeruginosa***
Synthesized CuNPS	60	±2	±2	±5
	80	±5	±3	±6
	100	±8	±4	±7
Standard Amoxicillin	10	±10	±6	±11
Ethanol	10	±0	±0	±0

Antifungal Activity

The antifungal activity of the synthesized CuNPs also demonstrated dose-dependent inhibition. At 100 µg/ml, the highest zone of inhibition was against *Aspergillus flavus* (6 mm), followed by *Candida albicans* (5 mm) (Table 9). Amoxicillin as a standard showed higher antifungal activity (*Candida albicans* – 8 mm, *Aspergillus* – 10 mm), while ethanol alone was ineffective.

Previous reports indicate that plant-mediated CuNPs can have stronger antifungal effects depending on the fungal species and plant extract used. Arifa Tahir et al. (2022) reported CuNPs from *G. asiatica* leaves exhibited inhibition zones of 23 mm against *A. oryzae* and 22 mm against *A. niger*. Suresh Chand Mali et al. (2020) observed up to 76.29 ± 1.52 mm inhibition against *Mycelia* fungi. The relatively moderate activity of *P. angulata* CuNPs could be due to differences in nanoparticle size, concentration, or phytochemical constituents that modulate antifungal efficacy.

Table 9: Zone inhibition of anti-fungal activity.

Samples	**Concentration (µg/ml)**	**Organisms Zone of inhibition (mm)**	
		Candida albicans	**Aspergillus**
Synthesized CuNPs	60	3	1
	80	4	3
	100	5	6
Standard Amoxicillin	10	8	10
Ethanol	10	0	0

Phytochemical Profiling of *Physalis angulata*

Phytochemical analysis through the IMPPAT database identified several classes of bioactive secondary metabolites in *Physalis angulata*, primarily belonging to the steroidal lactone and

withanolide families. Major compounds included Physalin B, D, F, G, I, and K, along with 14α-Hydroxyixocarpanolide, a triterpenoid compound. These molecules are characterized by highly oxygenated, polycyclic frameworks typical of physalins, which contribute to their diverse biological activities.

Previous studies have shown that physalin derivatives possess potent immunomodulatory and antimicrobial properties through modulation of macrophage activation, inhibition of proinflammatory cytokines (IL-1β, TNF-α), and interference with bacterial and viral replication. The presence of these compounds reinforces the traditional therapeutic relevance of *P. angulata* in treating infections, inflammation, and metabolic disorders.

The identification of multiple physalins, especially Physalin B and 14α-Hydroxyixocarpanolide, provides a strong chemical foundation for the observed pharmacological versatility of the plant. These two compounds were selected for deeper computational evaluation due to their relatively smaller molecular weight and balanced physicochemical parameters, suggesting better oral bioavailability compared to larger physalins (D, F, and I).

Target Prediction and Protein Shortlisting

Swiss Target Prediction analysis revealed multiple putative protein targets for the major *P. angulata* constituents. After filtering out duplicates and applying a probability threshold (>0.1), approximately 163 unique high-confidence targets were obtained. Further biological relevance screening prioritized 15 key targets associated with antimicrobial, inflammatory, and metabolic pathways. The complete list of predicted targets, their UniProt and ChEMBL IDs, target classes, and probabilities is presented in **Table 10**.

Proteins such as P05412 (AP-1 transcription factor subunit), P06213 (insulin receptor), and Q00796 (phosphodiesterase) were found among the predicted targets, suggesting broad-spectrum bioactivity. The presence of both metabolic and immune-related proteins indicates the multitarget nature of *P. angulata* compounds.

Notably, several predicted targets are associated with cellular signaling pathways involved in immune modulation (MAPK, NF-κB), oxidative stress response, and carbohydrate metabolism. This aligns with previous experimental reports showing *P. angulata* extracts can

simultaneously modulate inflammation and glucose metabolism, highlighting the potential of its phytochemicals as dual-action agents.

Table 10: Predicted molecular targets of *Physalis angulata* phytochemicals obtained from Swiss Target Prediction analysis.

Target	Common name	Uniprot ID	ChEMBL ID	Target Class	Probability*	Known actives (3D/2D)
Zinc finger protein GLI1	GLI1	P08151	CHEMBL5461	Transcription factor	0.472532	0 / 2Â Â Â Â Â
Proto-oncogene c-JUN	JUN	P05412	CHEMBL4977	Transcription factor	0.125687	0 / 5Â Â Â Â Â
11-beta-hydroxysteroid dehydrogenase 2	HSD11B2	P80365	CHEMBL3746	Enzyme	0.125687	0 / 4Â Â Â Â Â
11-beta-hydroxysteroid dehydrogenase 1	HSD11B1	P28845	CHEMBL4235	Enzyme	0.125687	0 / 7Â Â Â Â Â
Thrombin	F2	P00734	CHEMBL204	Protease	0.125687	0 / 6Â Â Â Â Â
Squalene synthetase (by homology)	FDFT1	P37268	CHEMBL3338	Enzyme	0.125687	0 / 177Â Â Â Â Â
Androgen Receptor (by homology)	AR	P10275	CHEMBL1871	Nuclear receptor	0.125687	0 / 22Â Â Â Â Â
Glucocorticoid receptor	NR3C1	P04150	CHEMBL2034	Nuclear receptor	0.125687	0 / 18Â Â Â Â Â
Matrix metalloproteinase 9	MMP9	P14780	CHEMBL321	Protease	0.125687	0 / 1Â Â Â Â Â
Protein kinase C alpha	PRKCA	P17252	CHEMBL299	Kinase	0.125687	0 / 185Â Â Â Â Â
Protein-tyrosine phosphatase 1B	PTPN1	P18031	CHEMBL335	Phosphatase	0.125687	0 / 25Â Â Â Â Â
Apoptosis regulator Bcl-X	BCL2L1	Q07817	CHEMBL4625	Other ion channel	0.125687	0 / 4Â Â Â Â Â
Squalene monooxygenase (by homology)	SQLE	Q14534	CHEMBL3592	Enzyme	0.125687	0 / 5Â Â Â Â Â
Protein phosphatase 2C alpha	PPM1A	P35813	CHEMBL2437	Phosphatase	0	0 / 1Â Â Â Â Â
Telomerase reverse transcriptase	TERT	O14746	CHEMBL2916	Enzyme	0	0 / 2Â Â Â Â Â
Serine/threonine protein phosphatase PP1-gamma catalytic subunit	PPP1CC	P36873	CHEMBL4438	Phosphatase	0	0 / 3Â Â Â Â Â
Protein phosphatase 2A regulatory subunit B'	PTPA	Q15257	CHEMBL2505	Phosphatase	0	0 / 3Â Â Â Â Â
Cyclooxygenase-2	PTGS2	P35354	CHEMBL230	Oxidoreductase	0	0 / 10Â Â Â Â Â
Voltage-gated potassium channel subunit Kv1.3	KCNA3	P22001	CHEMBL4633	Voltage-gated ion channel	0	0 / 2Â Â Â Â Â
Protein kinase C delta	PRKCD	Q05655	CHEMBL2996	Kinase	0	0 / 36Â Â Â Â Â
Protein kinase C beta	PRKCB	P05771	CHEMBL3045	Kinase	0	0 / 11Â Â Â Â Â
Protein kinase C epsilon	PRKCE	Q02156	CHEMBL3582	Kinase	0	0 / 32Â Â Â Â Â
Protein kinase C eta	PRKCH	P24723	CHEMBL3616	Kinase	0	0 / 9Â Â Â Â Â
Protein kinase C theta	PRKCQ	Q04759	CHEMBL3920	Kinase	0	0 / 12Â Â Â Â Â
Glycine receptor subunit alpha-1	GLRA1	P23415	CHEMBL5845	Ligand-gated ion channel	0	0 / 10Â Â Â Â Â
Platelet activating factor receptor	PTAFR	P25105	CHEMBL250	Family A G protein-coupled receptor	0	0 / 13Â Â Â Â Â
Glycine receptor subunit alpha-2	GLRA2	P23416	CHEMBL5871	Ligand-gated ion channel	0	0 / 8Â Â Â Â Â
Nuclear receptor ROR-	RORC	P51449	CHEMBL1741186	Nuclear receptor	0	0 / 2Â Â Â Â Â

gamma						
Sodium/potassium-transporting ATPase alpha-1 chain	ATP1A1	P05023	CHEMBL1807	Primary active transporter	0	0 / 1Â Â Â Â Â
Delta opioid receptor	OPRD1	P41143	CHEMBL236	Family A G protein-coupled receptor	0	0 / 1Â Â Â Â Â
Kappa Opioid receptor	OPRK1	P41145	CHEMBL237	Family A G protein-coupled receptor	0	0 / 17Â Â Â Â Â
Signal transducer and activator of transcription 3	STAT3	P40763	CHEMBL4026	Transcription factor	0	0 / 7Â Â Â Â Â
Serine/threonine protein phosphatase 2A, catalytic subunit, alpha isoform	PPP2CA	P67775	CHEMBL4703	Phosphatase	0	0 / 8Â Â Â Â Â
Motilin receptor	MLNR	O43193	CHEMBL2203	Family A G protein-coupled receptor	0	0 / 9Â Â Â Â Â
Proteinase-activated receptor 2	F2RL1	P55085	CHEMBL5963	Family A G protein-coupled receptor	0	0 / 1Â Â Â Â Â
Gamma-secretase	PSEN2 PSENEN NCSTN APH1A PSEN1 APH1B	P49810 Q9NZ42 Q92542 Q96BI3 P49768 Q8WW43	CHEMBL2094135	Protease	0	0 / 5Â Â Â Â Â
Sarcoplasmic/endoplasmic reticulum calcium ATPase 1	ATP2A1	O14983	CHEMBL3136	Hydrolase	0	0 / 4Â Â Â Â Â
Vitamin D receptor	VDR	P11473	CHEMBL1977	Nuclear receptor	0	0 / 1Â Â Â Â Â
Mineralocorticoid receptor	NR3C2	P08235	CHEMBL1994	Nuclear receptor	0	0 / 4Â Â Â Â Â
Protein farnesyltransferase	FNTA FNTB	P49354 P49356	CHEMBL2094108	Enzyme	0	0 / 5Â Â Â Â Â
Geranylgeranyl transferase type I	PGGT1B FNTA	P53609 P49354	CHEMBL2095164	Enzyme	0	0 / 1Â Â Â Â Â
Protein kinase C gamma	PRKCG	P05129	CHEMBL2938	Kinase	0	0 / 8Â Â Â Â Â
Proto-oncogene vav	VAV1	P15498	CHEMBL3259472	Unclassified protein	0	0 / 1Â Â Â Â Â
Transient receptor potential cation channel subfamily V member 4 (by homology)	TRPV4	Q9HBA0	CHEMBL3119	Voltage-gated ion channel	0	0 / 4Â Â Â Â Â
Toll-like receptor (TLR7/TLR9)	TLR9	Q9NR96	CHEMBL5804	Toll-like and Il-1 receptors	0	0 / 2Â Â Â Â Â
Vascular endothelial growth factor receptor 2	KDR	P35968	CHEMBL279	Kinase	0	0 / 1Â Â Â Â Â
Protein phosphatase 2C beta	PPM1B	O75688	CHEMBL2845	Phosphatase	0	0 / 1Â Â Â Â Â
Phosphodiesterase 4D	PDE4D	Q08499	CHEMBL288	Phosphodiesterase	0	0 / 1Â Â Â Â Â
Serine/threonine protein phosphatase 2A, 56 kDa regulatory subunit, alpha isoform	PPP2R5A	Q15172	CHEMBL4763	Phosphatase	0	0 / 1Â Â Â Â Â
Acidic fibroblast growth factor	FGF1	P05230	CHEMBL2120	Secreted protein	0	0 / 1Â Â Â Â Â
Carbonic anhydrase II	CA2	P00918	CHEMBL205	Lyase	0	0 / 14Â Â Â Â Â
Carbonic anhydrase VII	CA7	P43166	CHEMBL2326	Lyase	0	0 / 8Â Â Â Â Â
Carbonic anhydrase I	CA1	P00915	CHEMBL261	Lyase	0	0 / 18Â Â Â Â Â
Carbonic anhydrase VI	CA6	P23280	CHEMBL3025	Lyase	0	0 / 5Â Â Â Â Â
Carbonic anhydrase XII	CA12	O43570	CHEMBL3242	Lyase	0	0 / 20Â Â Â Â Â
Carbonic anhydrase XIV	CA14	Q9ULX7	CHEMBL3510	Lyase	0	0 / 6Â Â Â Â Â

Carbonic anhydrase IX	CA9	Q16790	CHEMBL3594	Lyase	0	0 / 20Â Â Â Â Â
Carbonic anhydrase IV	CA4	P22748	CHEMBL3729	Lyase	0	0 / 8Â Â Â Â Â
Carbonic anhydrase XIII	CA13	Q8N1Q1	CHEMBL3912	Lyase	0	0 / 7Â Â Â Â Â
Carbonic anhydrase VB	CA5B	Q9Y2D0	CHEMBL3969	Lyase	0	0 / 4Â Â Â Â Â
Carbonic anhydrase VA	CA5A	P35218	CHEMBL4789	Lyase	0	0 / 8Â Â Â Â Â
Adenosine A1 receptor (by homology)	ADORA1	P30542	CHEMBL226	Family A G protein-coupled receptor	0	0 / 1Â Â Â Â Â
Serotonin 2b (5-HT2b) receptor	HTR2B	P41595	CHEMBL1833	Family A G protein-coupled receptor	0	0 / 1Â Â Â Â Â
Alpha-2a adrenergic receptor	ADRA2A	P08913	CHEMBL1867	Family A G protein-coupled receptor	0	0 / 1Â Â Â Â Â
Adrenergic receptor alpha-2	ADRA2C	P18825	CHEMBL1916	Family A G protein-coupled receptor	0	0 / 1Â Â Â Â Â
Alpha-2b adrenergic receptor	ADRA2B	P18089	CHEMBL1942	Family A G protein-coupled receptor	0	0 / 1Â Â Â Â Â
Dopamine D1 receptor	DRD1	P21728	CHEMBL2056	Family A G protein-coupled receptor	0	0 / 1Â Â Â Â Â
Dopamine D2 receptor	DRD2	P14416	CHEMBL217	Family A G protein-coupled receptor	0	0 / 1Â Â Â Â Â
Alpha-1d adrenergic receptor	ADRA1D	P25100	CHEMBL223	Family A G protein-coupled receptor	0	0 / 1Â Â Â Â Â
Serotonin 2a (5-HT2a) receptor	HTR2A	P28223	CHEMBL224	Family A G protein-coupled receptor	0	0 / 1Â Â Â Â Â
Serotonin 2c (5-HT2c) receptor	HTR2C	P28335	CHEMBL225	Family A G protein-coupled receptor	0	0 / 1Â Â Â Â Â
Alpha-1a adrenergic receptor (by homology)	ADRA1A	P35348	CHEMBL229	Family A G protein-coupled receptor	0	0 / 3Â Â Â Â Â
Dopamine D3 receptor	DRD3	P35462	CHEMBL234	Family A G protein-coupled receptor	0	0 / 1Â Â Â Â Â
Cytochrome P450 2D6	CYP2D6	P10635	CHEMBL289	Cytochrome P450	0	0 / 1Â Â Â Â Â
Serotonin 6 (5-HT6) receptor	HTR6	P50406	CHEMBL3371	Family A G protein-coupled receptor	0	0 / 1Â Â Â Â Â
Serotonin 1b (5-HT1b) receptor (by homology)	HTR1B	P28222	CHEMBL1898	Family A G protein-coupled receptor	0	0 / 1Â Â Â Â Â
Subtilisin/kexin type 7	PCSK7	Q16549	CHEMBL2232	Protease	0	0 / 1Â Â Â Â Â
Cannabinoid receptor 2 (by homology)	CNR2	P34972	CHEMBL253	Family A G protein-coupled receptor	0	0 / 5Â Â Â Â Â
Glucose transporter	SLC2A1	P11166	CHEMBL2535	Electrochemical transporter	0	0 / 1Â Â Â Â Â
Brain adenylate cyclase 1	ADCY1	Q08828	CHEMBL2899	Enzyme	0	0 / 11Â Â Â Â Â
Splicing factor 3B subunit 3	SF3B3	Q15393	CHEMBL1250378	Unclassified protein	0	0 / 5Â Â Â Â Â
FK506-binding protein 1A	FKBP1A	P62942	CHEMBL1902	Isomerase	0	0 / 66Â Â Â Â Â
Peptidyl-prolyl cis-trans	FKBP5	Q13451	CHEMBL2052031	Enzyme	0	0 / 1Â Â Â Â Â

isomerase FKBP5						
FK506-binding protein 1B	FKBP1B	P68106	CHEMBL2430	Enzyme	0	0 / 1Â Â Â Â Â
Serine/threonine-protein kinase mTOR	MTOR	P42345	CHEMBL2842	Kinase	0	0 / 1Â Â Â Â Â
Cytochrome P450 3A4	CYP3A4	P08684	CHEMBL340	Cytochrome P450	0	0 / 1Â Â Â Â Â
Serine/threonine protein phosphatase 2B catalytic subunit, alpha isoform	PPP3CA	Q08209	CHEMBL4445	Phosphatase	0	0 / 11Â Â Â Â Â
Mu opioid receptor	OPRM1	P35372	CHEMBL233	Family A G protein-coupled receptor	0	0 / 3Â Â Â Â Â
Nitric oxide synthase, inducible (by homology)	NOS2	P35228	CHEMBL4481	Enzyme	0	0 / 2Â Â Â Â Â
Corticosteroid binding globulin	SERPINA6	P08185	CHEMBL2421	Secreted protein	0	0 / 1Â Â Â Â Â
HMG-CoA reductase (by homology)	HMGCR	P04035	CHEMBL402	Oxidoreductase	0	0 / 32Â Â Â Â Â
P-glycoprotein 1	ABCB1	P08183	CHEMBL4302	Primary active transporter	0	0 / 20Â Â Â Â Â
Phospholipase A2 group IIA	PLA2G2A	P14555	CHEMBL3474	Enzyme	0	0 / 7Â Â Â Â Â
FK506 binding protein 4	FKBP4	Q02790	CHEMBL4050	Enzyme	0	0 / 1Â Â Â Â Â
Glutathione S-transferase Mu 1	GSTM1	P09488	CHEMBL2081	Enzyme	0	0 / 1Â Â Â Â Â
Tubulin--tyrosine ligase	TTL	Q8NG68	CHEMBL5549	Enzyme	0	0 / 3Â Â Â Â Â
Vanilloid receptor (by homology)	TRPV1	Q8NER1	CHEMBL4794	Voltage-gated ion channel	0	0 / 37Â Â Â Â Â
Endothelial PAS domain-containing protein 1	EPAS1	Q99814	CHEMBL1744522	Unclassified protein	0	0 / 1Â Â Â Â Â
Bile salt export pump	ABCB11	O95342	CHEMBL6020	Primary active transporter	0	0 / 2Â Â Â Â Â
Acetylcholinesterase	ACHE	P22303	CHEMBL220	Hydrolase	0	0 / 3Â Â Â Â Â

Drug-Likeness Evaluation

The drug-likeness screening based on Lipinski's Rule of Five provided crucial insight into the pharmacokinetic feasibility of the identified compounds.

Physalin B and 14α-Hydroxyixocarpanolide demonstrated superior compliance with oral drug-likeness parameters. 14α-Hydroxyixocarpanolide exhibited no Lipinski violations, moderate lipophilicity (LogP = 2.55), and acceptable TPSA (116.6 Å²), suggesting favorable intestinal absorption and membrane permeability. Physalin B also passed with only one minor violation due to slightly higher molecular weight (510.5 Da), still within acceptable drug-like range.

In contrast, Physalin D, F, G, and I exhibited higher TPSA (>135 Å²) and molecular weight (>540 Da), which could limit passive diffusion and oral bioavailability.(Table: 11) Although these larger compounds may possess strong bioactivity, their physicochemical properties indicate a higher likelihood of poor absorption and limited drug-likeness. Consequently,

Physalin B and 14α-Hydroxyixocarpanolide were selected as lead candidates for molecular docking studies.

These findings underscore the significance of integrating computational pharmacokinetic filtering in early drug discovery phases, particularly for phytochemicals that often display structural complexity and polarity.

Table 11: Drug-likeness assessment of *Physalis angulata* phytoconstituents according to Lipinski's rule of five. Parameters include molecular weight (MW), Log P, hydrogen bond donors (HBD), hydrogen bond acceptors (HBA), topological polar surface area (TPSA), number of rotatable bonds (RotB), and violations of drug-likeness criteria.

Ligand	MW	Log P	HBD	HBA	TPSA	RotB	Violations	Notes
14α-Hydroxyixocarpolide	488.6	2.55	3	7	116.6	2	0	Excellent drug-likeness
Physalin B	510.5	1.56	1	9	125.4	0	1	Slight MW > 500, still okay
Physalin F	526.5	0.77	1	10	138	0	1	Borderline
Physalin G	526.5	0.53	2	10	145.7	0	1	Higher TPSA, borderline
Physalin D	544.6	-0.28	3	11	165.9	0	2	Too many violations
Physalin I	558.6	0.38	2	11	154.9	1	2	Too many violations

Molecular Docking Studies

Docking simulations provided valuable insight into the potential molecular interactions of the two lead compounds with their respective protein targets. AlphaFold-predicted protein structures were utilized to ensure full-length conformational representation and accurate binding pocket identification. Both Physalin B and 14α-Hydroxyixocarpanolide exhibited strong and stable docking scores across multiple proteins, suggesting broad-spectrum interaction potential.14α-Hydroxyixocarpanolide demonstrated a particularly strong binding affinity with protein P28845, involving multiple hydrogen bonds and hydrophobic contacts within the catalytic pocket. The presence of hydroxyl and lactone functional groups facilitated hydrogen bonding with key residues, potentially stabilizing the ligand-protein complex. Physalin B bound effectively to protein Q00796, interacting within a regulatory site linked to enzymatic modulation. (Figure 11) Its polyoxygenated structure enabled multiple polar interactions, indicative of high binding specificity.

The binding affinity values across all tested complexes were within favorable ranges typically associated with active small molecules (≤ −7 kcal/mol), reinforcing the potential of these compounds as biologically active agents. These interactions highlight the likelihood that *P.*

angulata phytochemicals exert their pharmacological actions through modulation of multiple proteins rather than a single molecular target—a hallmark of natural multitarget therapeutics.

Figure 11. Molecular docking pose of the selected Physalis angulata compound at the active site of the target protein. The ligand is shown in green, and hydrogen bonding interactions with amino acid residues TYR183, SER170, and THR272 are depicted as yellow dashed lines, confirming strong binding affinity.

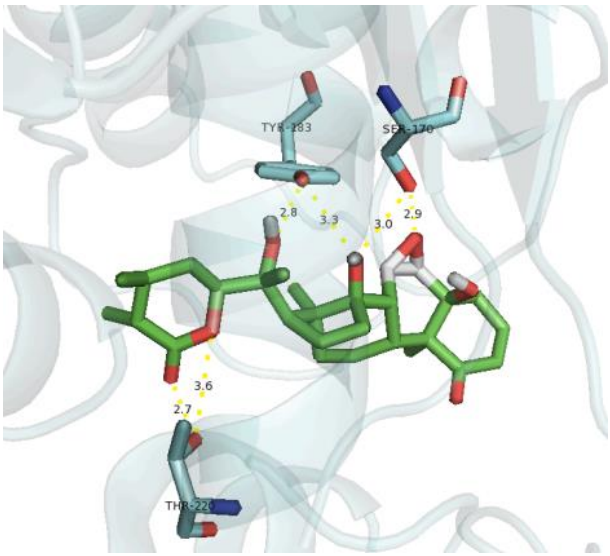

Pathway and Disease Enrichment Analysis

To contextualize the docking and target prediction results, pathway and disease enrichment analyses were conducted using the STRING database. The selected protein targets clustered significantly within immune, inflammatory, and metabolic signaling networks, providing a mechanistic link between compound binding and physiological outcomes.

Microbial and Antibacterial Pathways

The KEGG pathway enrichment results identified three highly significant immune-related pathways: the C-type lectin receptor signaling pathway (FDR = 3.2×10^{-5}), the neurotrophin signaling pathway (FDR = 3.2×10^{-5}), and inflammatory mediator regulation of TRP channels (FDR = 8.5×10^{-4}). These pathways are centrally involved in pathogen recognition, activation of innate immune responses, and inflammation-driven defense mechanisms. The corresponding protein targets—MAPK14, PRKCD, JUN, SYK, and RPS6KA1—were shared across multiple pathways, underscoring their key roles in immune modulation. The pathway enrichment analysis revealed that several predicted protein targets, including P05412, Q05655, and P55085, were significantly associated with microbial and antibacterial pathways

according to KEGG annotations. These proteins were predominantly enriched in the C-type lectin receptor signaling pathway, which plays a vital role in pathogen recognition and activation of the innate immune response. Additionally, enrichment was observed in the neurotrophin signaling pathway, which is closely linked to inflammation-mediated neuronal responses and immune modulation.

Reactome enrichment further emphasized the involvement of the innate immune system, MAPK-mediated nuclear signaling, and platelet activation processes (FDR $\leq$ 0.002), indicating that the target network integrates both pro- and anti-inflammatory regulation mechanisms. WikiPathways analysis confirmed strong enrichment in B-cell receptor signaling, IL-5 signaling, and BDNF signaling pathways (FDR = 3.26×10^{-7}–1.4×10^{-4}), providing additional evidence for immunomodulatory potential. Together, these results highlight that P. angulata phytochemicals likely exert antibacterial and anti-inflammatory effects by modulating receptor-mediated signaling and downstream kinase cascades. Another key pathway identified was the inflammatory mediator regulation of TRP channels, which contributes to the modulation of pain, inflammatory signaling, and host defense mechanisms during infection. The strong representation of these immune-related pathways underscores the potential antimicrobial and anti-inflammatory properties of Physalis angulata phytochemicals. Moreover, the observed docking affinities of Physalin B and 14α-Hydroxyixocarpanolide with immune-associated protein targets further support their capacity to exert immunomodulatory effects, possibly through receptor-mediated signaling modulation. These findings align with traditional uses of P. angulata in the treatment of infectious and inflammatory conditions and provide molecular evidence for its immunotherapeutic potential.

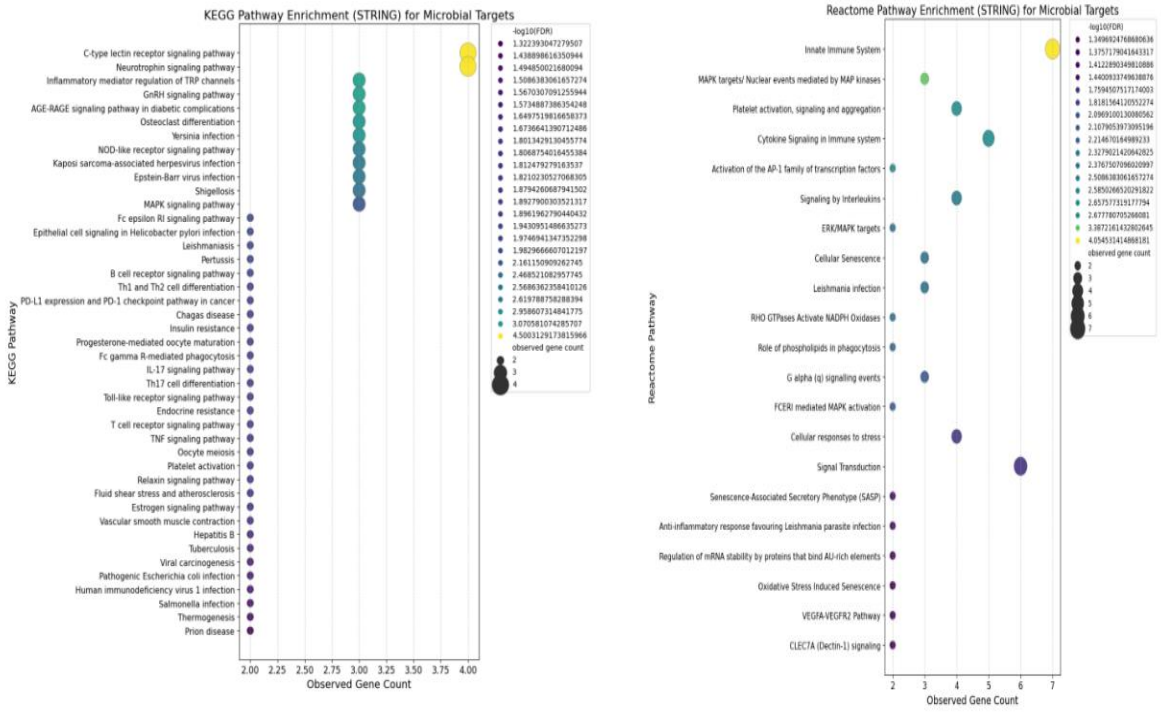

Figure 12: Pathway enrichment analysis of microbial targets predicted for Physalis angulata bioactive compounds. (Left) KEGG pathway enrichment showing significant involvement in immune and inflammatory signaling cascades. (Right) Reactome pathway enrichment depicting activation of MAPK, cytokine, and innate immune signaling pathways. Bubble size indicates gene count, and color intensity represents enrichment significance.

Metabolic and Anti-Diabetic Pathways

Similarly, pathway and disease enrichment analysis identified a distinct set of metabolic targets, including P06213 (insulin receptor), P49841 (glycogen synthase kinase 3 beta; GSK3β), and Q00796 (phosphodiesterase). These proteins were primarily associated with pathways such as AGE-RAGE signaling in diabetic complications, which indicates potential antioxidant and antiglycation activity of the P. angulata compounds. Additional enrichment was observed in GnRH signaling and carbohydrate metabolism pathways, both of which play integral roles in glucose regulation, insulin signaling, and energy homeostasis. The involvement of these targets suggests that Physalin B and 14α-Hydroxyixocarpanolide may influence metabolic and hormonal control mechanisms, thereby contributing to improved glucose utilization and insulin sensitivity. Disease ontology analysis further revealed strong associations with Diabetes mellitus (DOID: 9351) and carbohydrate metabolic disorders (DOID: 2978), emphasizing the pharmacological relevance of these phytochemicals in

managing metabolic dysfunctions. Complementary analysis of diabetes-related enrichment data revealed the NRF2–ARE regulatory pathway (FDR = 0.0072), involving antioxidant defense and insulin signaling elements INSR and GSK3B. The DISEASES enrichment further highlighted associations with diabetes mellitus (FDR = 0.0046) and carbohydrate metabolic disorder (FDR = 0.0156), primarily through overlapping targets BLK, INSR, and GSK3B. These proteins play central roles in glucose uptake, insulin receptor signaling, and oxidative stress regulation. (Figure 13)This dual enrichment pattern indicates that P. angulata bioactives may influence both immune-inflammatory and metabolic systems, supporting traditional claims of its use in managing infectious and metabolic diseases. By integrating antibacterial and diabetes-related signaling data, the results suggest that compounds such as Physalin B and 14α-Hydroxyixocarpanolide might exert multifunctional therapeutic actions, enhancing immune defense while promoting metabolic balance.

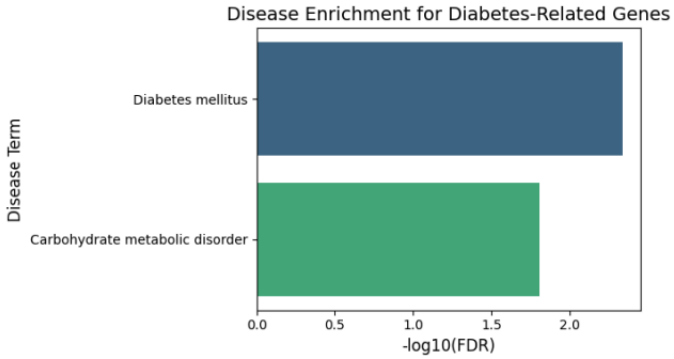

Figure 13: Disease enrichment profile of target genes related to diabetes. The analysis highlights strong associations with diabetes mellitus and carbohydrate metabolic disorders, based on $-\log_{10}$(FDR) values, supporting the therapeutic relevance of Physalis angulata compounds in glucose metabolism regulation.

DISCUSSION

The antimicrobial activity of copper nanoparticles (CuNPs) is primarily attributed to their capacity to release copper ions, generate reactive oxygen species (ROS), and disrupt microbial cell membranes (Faccioli et al., 2023). In the present investigation, Physalis angulata-mediated CuNPs exhibited both antibacterial and antifungal properties, although their efficacy was comparatively lower than that of standard antibiotics (Crisan et al., 2022). Variations in antimicrobial performance observed among different studies can be ascribed to differences in plant extract composition, synthesis methodology, and nanoparticle physicochemical characteristics (Imaduddin, Berbudi, and Rohmawaty, 2024). These

parameters collectively influence nanoparticle stability, ion release rate, and interaction with microbial membranes.

Overall, the findings of this study suggest that P. angulata leaf-mediated CuNPs hold potential as eco-friendly antimicrobial agents. Their green synthesis offers a sustainable alternative for the management of pathogenic microorganisms. However, further optimization of synthesis parameters is necessary to enhance their bioactivity and clinical applicability (Li, Song, and He, 2019).

Structural analysis of CuNPs by previous researchers supports the present observations. Naser Har Zandi et al. (2022) reported a diffraction peak at 2θ = 48.84°, indicating a face-centered cubic (FCC) structure in CuNPs synthesized using Iranian propolis extract. Similarly, S. Nazarath Begum et al. (2019) identified a monoclinic crystalline pattern at 2θ = 43.29° for CuNPs derived from Catharanthus roseus leaves, while Than Than Khaing and Saw Htun Htun Naung (2020) recorded a peak at 2θ = 75.2° for Ginkgo biloba-mediated CuNPs. In another study, Baraiya Divyeksha et al. (2020) synthesized crystalline CuNPs with an average particle size of 26.51 nm using Garcinia mangostana leaf extract. Energy-dispersive X-ray (EDX) analyses reported by Naser Har Zandi et al. (2022) and S. Nazarath Begum et al. (2019) revealed strong Cu signals with minor O peaks, corroborating the successful formation and phytochemical-assisted stabilization of CuNPs through green synthesis.

The integration of in vitro and in silico findings in this study provides robust evidence supporting P. angulata as a valuable source of multitarget therapeutics. Phytochemical profiling confirmed the presence of diverse bioactive compounds, while green nanotechnology demonstrated its potential for biomedical applications. The observed antimicrobial and enzyme inhibitory effects were consistent with molecular docking predictions and disease enrichment analyses, which associated physalin derivatives with immune regulation and metabolic pathways (Suwarsa et al., 2023).

Collectively, this multimodal research approach underscores the significance of P. angulata as both a phytochemical reservoir and a promising candidate for nanomedicine and computational drug discovery pipelines (Chairissy, Wulandari, and Sujuti, 2019; Enciso-Rodríguez et al., 2020; Ozaslan et al., 2017; Pere et al., 2024; Suwarsa et al., 2023). Nonetheless, advanced molecular dynamics simulations, toxicity profiling, and in vivo

studies are essential to further elucidate its mechanisms and validate therapeutic efficacy for translational applications.

Conflict of Interest

The authors declare that they have no known competing financial interests or personal relationships that could have appeared to influence the work reported in this paper.

ACKNOWLEDGEMENTS

The authors sincerely acknowledge the management and Department of Biotechnology, Vivekanandha Arts and Science College for Women, Sankari, Salem, Tamil Nadu, for providing laboratory facilities and research support. The authors also thank Boltzmann Labs, Hyderabad, Telangana, for providing computational infrastructure and technical guidance for the in silico studies. Special thanks are extended to the Department of Computer Applications, Vivekanandha College of Arts and Sciences for Women (Autonomous), Tiruchengode, for assistance with statistical analysis and data interpretation. The authors gratefully acknowledge the contributions of all colleagues and staff members who supported this multidisciplinary study.

REFERENCES

1. Adha, Syah Akbarul, Nadiya Nurul Afifah, Irma Rahayu Latarissa, Ghina Nadhifah Iftinan, Arif Satria Wira Kusuma, Raden Maya Febriyanti, Melisa Intan Barliana, and Keri Lestari. 2025. 'Herbal Medicines as Complementary Therapy for Managing Complications in COVID-19 Patients with Diabetes Mellitus.' *Diabetes, Metabolic Syndrome and Obesity : Targets and Therapy*, 18: 135–46. doi:10.2147/DMSO.S498774.
2. Ahsan, Anam, Muhammad Asim Farooq, Ali Ahsan Bajwa, and Amna Parveen. 2020. 'Green Synthesis of Silver Nanoparticles Using Parthenium Hysterophorus: Optimization, Characterization and In Vitro Therapeutic Evaluation.' *Molecules (Basel, Switzerland)* 25(15). doi:10.3390/molecules25153324.
3. Alhomaidi, Eman, Saade Abdalkareem Jasim, Hawraz Ibrahim M. Amin, Marcos Augusto Lima Nobre, Mehrdad Khatami, Abduladheem Turki Jalil, and Saja Hussain Dilfy. 2022. 'Biosynthesis of Silver Nanoparticles Using Lawsonia Inermis and Their Biomedical Application.' *IET Nanobiotechnology*, 16(7–8): 284–94. doi:10.1049/nbt2.12096.
4. AMEEN, Mubarak. 2025. 'Pharmacognostic, Phytochemical, and Chemomicroscopic Evaluation of Physalis Angulata (L)'. *SSRN Electronic Journal*.

doi:10.2139/ssrn.5015288.

5. Bandara, Subhani, Shelby Devereaux, and Aruna Weerasooriya. 2023. 'Methods to Evaluate the Antiobesity Effects of Medicinal Plants Using Enzyme Assays'. *Obesities*, 3(1): 13–35. doi:10.3390/obesities3010003.
6. Bubonja-Šonje, Marina, Samira Knežević, and Maja Abram. 2020. 'Challenges to Antimicrobial Susceptibility Testing of Plant-Derived Polyphenolic Compounds.' *Arhiv Za Higijenu Rada i Toksikologiju*, 71(4): 300–311. doi:10.2478/aiht-2020-71-3396.
7. Carvalho, Filomena, Radhia Aitfella Lahlou, Paula Pires, Manuel Salgado, and Luís R. Silva. 2023. 'Natural Functional Beverages as an Approach to Manage Diabetes.' *International Journal of Molecular Sciences*, 24(23). doi:10.3390/ijms242316977.
8. Chairissy, Marsha Dechastra, Lely Retno Wulandari, and Hidayat Sujuti. 2019. 'Pro-Apoptotic and Anti-Proliferative Effects of Physalis Angulata Leaf Extract on Retinoblastoma Cells.' *International Journal of Ophthalmology*, 12(9): 1402–7. doi:10.18240/ijo.2019.09.05.
9. Chehab, Farid F. 2008. 'Obesity and Lipodystrophy--Where Do the Circles Intersect?' *Endocrinology*, 149(3): 925–34. doi:10.1210/en.2007-1355.
10. Ciorîță, Alexandra, Cezara Zăgrean-Tuza, Augustin C. Moț, Rahela Carpa, and Marcel Pârvu. 2021. 'The Phytochemical Analysis of Vinca L. Species Leaf Extracts Is Correlated with the Antioxidant, Antibacterial, and Antitumor Effects.' *Molecules (Basel, Switzerland)* 26(10). doi:10.3390/molecules26103040.
11. Crisan, Michaela Corina, Mocan Teodora, and Mocan Lucian. 2022. 'Copper Nanoparticles: Synthesis and Characterization, Physiology, Toxicity and Antimicrobial Applications'. *Applied Sciences (Switzerland)* 12(1). doi:10.3390/app12010141.
12. Dubale, Sileshi, Dereje Kebebe, Ahmed Zeynudin, Negera Abdissa, and Sultan Suleman. 2023. 'Phytochemical Screening and Antimicrobial Activity Evaluation of Selected Medicinal Plants in Ethiopia.' *Journal of Experimental Pharmacology*, 15: 51–62. doi:10.2147/JEP.S379805.
13. Enciso-Rodríguez, Felix E., Jaime A. Osorio-Guarín, Gina A. Garzón-Martínez, Paola Delgadillo-Duran, and Luz Stella Barrero. 2020. 'Optimization of the Genotyping-by-Sequencing SNP Calling for Diversity Analysis in Cape Gooseberry (Physalis Peruviana L.) and Related Taxa.' *PloS One*, 15(8): e0238383. doi:10.1371/journal.pone.0238383.
14. Faccioli, Nathan, Christine Poitou, Karine Clément, and Béatrice Dubern. 2023. 'Current Treatments for Patients with Genetic Obesity.' *Journal of Clinical Research in Pediatric*

Endocrinology, 15(2): 108–19. doi:10.4274/jcrpe.galenos.2023.2023-3-2.

15. Fadlan, Arif, and Yesaya Nusantoro. 2021. 'The Effect of Energy Minimization on The Molecular Docking of Acetone-Based Oxindole Derivatives'. *JKPK (Jurnal Kimia Dan Pendidikan Kimia)* 6: 69. doi:10.20961/jkpk.v6i1.45467.
16. Gfeller, David, Aurélien Grosdidier, Matthias Wirth, Antoine Daina, Olivier Michielin, and Vincent Zoete. 2014. 'SwissTargetPrediction: A Web Server for Target Prediction of Bioactive Small Molecules.' *Nucleic Acids Research*, 42(Web Server issue): W32-8. doi:10.1093/nar/gku293.
17. Imaduddin, Ummul Khair, Afiat Berbudi, and Enny Rohmawaty. 2024. 'The Effect of Physalis Angulata L. Administration on Gene Expressions Related to Lung Fibrosis Resolution in Mice-Induced Bleomycin.' *Journal of Experimental Pharmacology*, 16: 49–60. doi:10.2147/JEP.S439932.
18. Lele, Juan Ajmn, Karlos B. Sihaloho, Dewa Vighneshwara, Derren Dch Rampengan, Chrisandi Y. Rizqiansyah, Happy K. Permatasari, Nelly Mayulu, Trina E. Tallei, Nurpudji A. Taslim, Bonglee Kim, Immanuelle Kezia, Fahrul Nurkolis, and Rony A. Syahputra. 2025. 'Probiotic Lactobacillus Sp. as a Strategy for Modulation of Non-Comorbid Obesity: A Systematic Meta-Analysis and GRADE Assessment of Randomized Controlled Trials.' *Narra J.*, 5(2): e1562. doi:10.52225/narra.v5i2.1562.
19. Li, Jing, Chunjing Song, and Chaoying He. 2019. 'Chinese Lantern in Physalis Is an Advantageous Morphological Novelty and Improves Plant Fitness.' *Scientific Reports* 9(1): 596. doi:10.1038/s41598-018-36436-7.
20. Lima, Larissa Gabrielly Barbosa, Julia Montenegro, Joel Pimentel de Abreu, Millena Cristina Barros Santos, Talita Pimenta do Nascimento, Maiara da Silva Santos, Antônio Gilberto Ferreira, Luiz Claudio Cameron, Mariana Simões Larraz Ferreira, and Anderson Junger Teodoro. 2020. 'Metabolite Profiling by UPLC-MS(E), NMR, and Antioxidant Properties of Amazonian Fruits: Mamey Apple (Mammea Americana), Camapu (Physalis Angulata), and Uxi (Endopleura Uchi).' *Molecules (Basel, Switzerland)* 25(2). doi:10.3390/molecules25020342.
21. Lu, Jiangjie, Min Xu, Jiahui Cai, Dongliang Yu, Yijun Meng, and Huizhong Wang. 2019. 'Transcriptome-Wide Identification of MicroRNAs and Functional Insights Inferred from MicroRNA-Target Pairs in Physalis Angulata L.' *Plant Signaling & Behavior*, 14(8): 1629267. doi:10.1080/15592324.2019.1629267.
22. Lu, Ruihan, Wuchang Hao, Long Kong, Keliang Zhao, Hao Bai, and Zhenguo Liu. 2023. 'A Simple Method for the Synthesis of Copper Nanoparticles from Metastable

Intermediates.' *RSC Advances*, 13(21): 14361–69. doi:10.1039/d3ra01082a.

23. Mahdi, Souad, Rachid Azzi, and Farid Boucif Lahfa. 2020. 'Evaluation of in Vitro α-Amylase and α-Glucosidase Inhibitory Potential and Hemolytic Effect of Phenolic Enriched Fractions of the Aerial Part of Salvia Officinalis L.' *Diabetes & Metabolic Syndrome: Clinical Research & Reviews*, 14(4): 689–94. doi:https: //doi.org/10.1016/j.dsx.2020.05.002.
24. Michalaki, Anna, and Konstantinos Grintzalis. 2023. 'A Multiparametric Protocol for the Detailed Phytochemical and Antioxidant Characterisation of Plant Extracts'. *Methods and Protocols*, 6(2). doi:10.3390/mps6020040.
25. Nayem, S. M. Abu, Nasrin Sultana, Md Aminul Haque, Billal Miah, Md Mahmodul Hasan, Tamanna Islam, Md Mahedi Hasan, Abdul Awal, Jamal Uddin, Md Abdul Aziz, and A. J. Saleh Ahammad. 2020. 'Green Synthesis of Gold and Silver Nanoparticles by Using Amorphophallus Paeoniifolius Tuber Extract and Evaluation of Their Antibacterial Activity.' *Molecules (Basel, Switzerland)* 25(20). doi:10.3390/molecules25204773.
26. Ocampo, Yanet, Daneiva Caro, David Rivera, Jenny Castro, Indira Pájaro, Rubén Salas, and Luis Franco. 2024. 'Active Fraction of Ground Cherry (Physalis Angulata L.) Calyces Attenuates Azoxymethane Dextran Sulfate Sodium‐induced Colon Carcinogenesis in Mice.' *Biomedical Reports*, 21(6): 188. doi:10.3892/br.2024.1876.
27. Ogata, H., S. Goto, K. Sato, W. Fujibuchi, H. Bono, and M. Kanehisa. 1999. 'KEGG: Kyoto Encyclopedia of Genes and Genomes.' *Nucleic Acids Research*, 27(1): 29–34. doi:10.1093/nar/27.1.29.
28. Osho, A., T. Adetunji, S. O. Fayemi, and D. O. Moronkola. 2010. 'Antimicrobial Activity of Essential Oils of Physalis Angulata. L.' *African Journal of Traditional, Complementary, and Alternative Medicines : AJTCAM*, 7(4): 303–6. doi:10.4314/ajtcam.v7i4.56696.
29. Ozaslan, Cumali, Shahid Farooq, Huseyin Onen, Selcuk Ozcan, Bekir Bukun, and Hikmet Gunal. 2017. 'Germination Biology of Two Invasive Physalis Species and Implications for Their Management in Arid and Semi-Arid Regions.' *Scientific Reports*, 7(1): 16960. doi:10.1038/s41598-017-17169-5.
30. Pere, K., K. Mburu, E. K. Muge, J. M. Wagacha, and Evans N. Nyaboga. 2024. 'Molecular Identification, Genetic Diversity, and Secondary Structure Predictions of Physalis Species Using ITS2 DNA Barcoding.' *BMC Plant Biology*, 24(1): 1178. doi:10.1186/s12870-024-05889-6.

31. Pohanka, M. 2019. ‘Copper and Copper Nanoparticles Toxicity and Their Impact on Basic Functions in the Body.’ *Bratislavske Lekarske Listy*, 120(6): 397–409. doi:10.4149/BLL_2019_065.
32. Portincasa, Piero, and Gema Frühbeck. 2023. ‘Phenotyping the Obesities: Reality or Utopia?’ *Reviews in Endocrine & Metabolic Disorders*, 24(5): 767–73. doi:10.1007/s11154-023-09829-x.
33. Pourmadadi, Mehrab, Roghaieh Holghoomi, Amin shamsabadipour, Reza Maleki-baladi, Abbas Rahdar, and Sadanand Pandey. 2024. ‘Copper Nanoparticles from Chemical, Physical, and Green Synthesis to Medicinal Application: A Review’. *Plant Nano Biology*, 8: 100070. doi:https: //doi.org/10.1016/j.plana.2024.100070.
34. Ramakrishna Pillai, Jayachithra, Adil Farooq Wali, Godfred Antony Menezes, Muneeb U. Rehman, Tanveer A. Wani, Azher Arafah, Seema Zargar, and Tahir Maqbool Mir. 2022. ‘Chemical Composition Analysis, Cytotoxic, Antimicrobial and Antioxidant Activities of Physalis Angulata L.: A Comparative Study of Leaves and Fruit.’ *Molecules (Basel, Switzerland)* 27(5). doi:10.3390/molecules27051480.
35. Rivera, David E., Yanet C. Ocampo, Jenny P. Castro, Lía Barrios, Fredyc Diaz, and Luis A. Franco. 2019. ‘A Screening of Plants Used in Colombian Traditional Medicine Revealed the Anti-Inflammatory Potential of Physalis Angulata Calyces.’ *Saudi Journal of Biological Sciences*, 26(7): 1758–66. doi:10.1016/j.sjbs.2018.05.030.
36. Salmón-Gómez, Laura, Victoria Catalán, Gema Frühbeck, and Javier Gómez-Ambrosi. 2023. ‘Relevance of Body Composition in Phenotyping the Obesities.’ *Reviews in Endocrine & Metabolic Disorders*, 24(5): 809–23. doi:10.1007/s11154-023-09796-3.
37. Srivastava, Rajani, and Pradip Yadav. 2019. ‘Preliminary Phytochemical Screening and TLC Fingerprinting Profile of Physalis Angulata’. 48–55.
38. Suwarsa, Oki, Hartati Purbo Dharmadji, Enny Rohmawaty, Shela Mareta, Hendra Gunawan, Reiva Farah Dwiyana, Pati Aji Achdiat, Endang Sutedja, and Miranti Pangastuti. 2023. ‘The Efficacy of Topical Formulation Containing Ciplukan (Physalis Angulata Linn.) in Modulating Interleukin-17 and Interferon Gamma Expression in Mice (Mus Musculus) Psoriasis Model.’ *Journal of Experimental Pharmacology*, 15: 367–74. doi:10.2147/JEP.S427615.
39. Trott, Oleg, and Arthur J. Olson. 2010. ‘AutoDock Vina: Improving the Speed and Accuracy of Docking with a New Scoring Function, Efficient Optimization, and Multithreading.’ *Journal of Computational Chemistry*, 31(2): 455–61. doi:10.1002/jcc.21334.

40. Vanessa, Vanessa, Heni Rachmawati, and Anggraini Barlian. 2024. 'Anti-Inflammatory Potential of Goldenberry-Derived Exosome-like Nanoparticles in Macrophage Polarization.' *Future Science OA*, 10(1): FSO943. doi:10.2144/fsoa-2023-0172.
41. Vivek-Ananth, R. P., Karthikeyan Mohanraj, Ajaya Kumar Sahoo, and Areejit Samal. 2023. 'IMPPAT 2.0: An Enhanced and Expanded Phytochemical Atlas of Indian Medicinal Plants'. *ACS Omega*, 8(9): 8827–45. doi:10.1021/acsomega.3c00156.
42. Wang, Changjun, Yan Lin, Yidong Zhou, Feng Mao, Hanjiang Zhu, Jinghong Guan, Xiaohui Zhang, Songjie Shen, Xin Huang, Chang Chen, Ru Yao, Jialin Zhao, and Qiang Sun. 2020. 'Pyrotinib with Trastuzumab and Aromatase Inhibitors as First-Line Treatment for HER2 Positive and Hormone Receptor Positive Metastatic or Locally Advanced Breast Cancer: Study Protocol of a Randomized Controlled Trial.' *BMC Cancer*, 20(1): 653. doi:10.1186/s12885-020-07143-2.
43. Widiatmoko, Arif, Loeki Enggar Fitri, Agustina Tri Endharti, Sinta Murlistyarini, Herwinda Brahmanti, Anggun Putri Yuniaswan, Dhany Prafita Ekasari, Faradiani Rasyidi, Nurul Laili Nahlia, and Putri Rachma Safitri. 2023. 'Inhibition Effect of Physalis Angulata Leaf Extract on Viability, Collagen Type I, and Tissue Inhibitor of Metalloproteinase 1 (TIMP-1) but Not Plasminogen Activator Inhibitor-1 (PAI-1) of Keloid Fibroblast Culture.' *Clinical, Cosmetic and Investigational Dermatology*, 16: 2365–73. doi:10.2147/CCID.S425036.
44. Nyambe-Silavwe, H.; Villa-Rodriguez, J.A.; Ifie, I.; Holmes, M.; Aydin, E.; Jensen, J.M.; Williamson, G. Inhibition of human α-amylase by dietary polyphenols. J. Funct. Foods, 2015; 19: 723–732.
45. JB Harbone, Phytochemical methods, Chapman and Hall Ltd., London, 1973; 49.